Monthly Notices
of the
ROYAL ASTRONOMICAL SOCIETY

MNRAS **499,** 5915–5931 (2020)
Advance Access publication 2020 October 16

doi:10.1093/mnras/staa3195

Polarimetric and radiative transfer modelling of HD 172555

Jonathan P. Marshall [1,2★] Daniel V. Cotton [2,3,4] Peter Scicluna [1,5] Jeremy Bailey [6] Lucyna Kedziora-Chudczer[2] and Kimberly Bott[7]

[1]*Academia Sinica, Institute of Astronomy and Astrophysics, 11F Astronomy-Mathematics Building, NTU/AS campus, No. 1, Section 4, Roosevelt Rd., Taipei 10617, Taiwan*
[2]*University of Southern Queensland, Centre for Astrophysics, Toowoomba, QLD 4350, Australia*
[3]*Anglo Australian Telescope, Australian National University, 418 Observatory Road, Coonabarabran, NSW 2357, Australia*
[4]*Western Sydney University, Locked Bag 1797, Penrith-South DC, NSW 1797, Australia*
[5]*European Southern Observatory, Alonso de Cordova 3107, Santiago RM, Chile*
[6]*School of Physics, University of New South Wales, Sydney, NSW 2052, Australia*
[7]*Department of Earth and Planetary Science, University of California, Riverside, CA 92521, USA*

Accepted 2020 October 5. Received 2020 October 5; in original form 2020 July 16

ABSTRACT

The debris disc around HD 172555 was recently imaged in near-infrared polarized scattered light by the Very Large Telescope's Spectro-Polarimetric High-contrast Exoplanet REsearch instrument. Here we present optical aperture polarization measurements of HD 172555 by the HIgh Precision Polarimetric Instrument (HIPPI), and its successor HIPPI-2 on the Anglo-Australian Telescope. We seek to refine constraints on the disc's constituent dust grains by combining our polarimetric measurements with available infrared and millimetre photometry to model the scattered light and continuum emission from the disc. We model the disc using the 3D radiative transfer code HYPERION, assuming the orientation and extent of the disc as obtained from the SPHERE observation. After correction for the interstellar medium contribution, our multiwavelength HIPPI/-2 observations (both magnitude and orientation) are consistent with the recent SPHERE polarization measurement with a fractional polarization $p = 62.4 \pm 5.2$ ppm at 722.3 nm, and a position angle $\theta = 67^\circ \pm 3^\circ$. The multiwavelength polarization can be adequately replicated by compact, spherical dust grains (i.e. from Mie theory) that are around 1.2 μm in size, assuming astronomical silicate composition, or 3.9 μm, assuming a composition derived from radiative transfer modelling of the disc. We were thus able to reproduce both the spatially resolved disc emission and polarization with a single grain composition model and size distribution.

Key words: circumstellar matter – polarization – radiative transfer – stars: individual: HD 172555.

1 INTRODUCTION

HD 172555 is a young, A7 V type star with a bright, warm debris disc ($L_{\rm dust}/L_\star = 7.72 \times 10^{-4}$, $T_{\rm dust} = 285$ K; Cotten & Song 2016). As a member of the β Pictoris moving group, the system has a well-determined age of 23 ± 3 Myr (Mamajek & Bell 2014). The inclination and orientation of the debris disc around HD 172555 were first constrained at mid-infrared wavelengths through combining MIDI interferometric measurements with reanalysis of mid-infrared continuum observations taken by the TReCS instrument (Moerchen, Telesco & Packham 2010; Smith, Wyatt & Haniff 2012). Recently, Engler et al. (2018) directly imaged the disc in scattered light using SPHERE/ZIMPOL polarimetry. They found the high-inclination orientation ($i = 103.^\circ5$, $\phi = 112.^\circ3$) and measured an outer extent of 8.5–11.3 AU for the disc. They also determined a lower limit to the polarization of 62 ± 6 ppm in the VBB filter ($\lambda_c = 735$ nm, $\Delta\lambda = 290$ nm).

The substantial mid-infrared continuum emission observed by *Spitzer* was identified as being anomalous due its brightness, and inconsistent with a steady-state origin for the circumstellar debris (Wyatt et al. 2007). Unusually for a debris disc, the *Spitzer*/IRS mid-infrared spectrum of HD 172555 shows features, including SiO gas, consistent with the dust grains originating in a high-velocity impact (Lisse et al. 2009; Johnson et al. 2012). Based on infrared spectroscopy, the dust composition is inferred to be differentiated silicate material similar to Asterodial bodies in the Solar system (Morlok et al. 2012). High-resolution stellar spectroscopy has also revealed variable absorption in ultraviolet and optical lines, interpreted as evidence of cometary activity in the system (Kiefer et al. 2014; Grady et al. 2018). Multiepoch mid-infrared spectroscopic observations of HD 172555 show no substantial change (<20 per cent) in the shape of the 10-μm silicate feature, suggesting the submicron dust grain population is stable on decadal time-scales (Su et al. 2020). At far-infrared wavelengths, *Herschel* photometric and spectroscopic observations revealed the presence of gas in the disc through detection of 63-μm [O I] emission, but no evidence of a second cool dust component in the system (Riviere-Marichalar et al. 2012, 2014). Overall, these observations present a picture of a system in a state of dynamic disarray undergoing some collisional violence.

Here we present multiwavelength optical aperture polarimetric measurements of HD 172555 taken with the HIgh Precision Polarimetric Instrument (HIPPI; Bailey et al. 2015), and its successor

★ E-mail: jmarshall@asiaa.sinica.edu.tw

HIPPI-2 (Bailey et al. 2020a), on the 3.9-m Anglo-Australian Telescope (AAT). These observations record the scattering-induced polarization signature of debris dust around HD 172555. Combining these measurements with the architecture, as determined by the SPHERE/ZIMPOL observations, and ancillary mid- and far-infrared photometry measurements tracing the thermal emission from the dust, we seek to better constrain the size and albedo of the disc's constituent dust grains (following e.g. Choquet et al. 2018; Marshall et al. 2018). The results of our analysis are compared to the values expected for dust grains present in the disc inferred from the presence of spectral features in the mid-infrared spectrum.

The remainder of this paper is laid out as follows. We present the multiwavelength HIPPI/-2 polarimetric observations in Section 2. The impact of polarization induced by dust in the interstellar medium is dealt with in Section 3. We combine the ISM-subtracted polarimetric measurements with archival photometric data to produce a self-consistent model of the disc's scattered light and continuum emission in Section 4. A comparison of our results with the dust composition inferred from the mid-infrared spectrum is given in Section 5. Finally, we present our conclusions in Section 6.

2 OBSERVATIONS

2.1 Ancilliary data

The stellar parameters used in this work, including the luminosity, effective temperature, and radius, were taken from Gaia Collaboration et al. (2018); a summary of the stellar parameters adopted for this work along with some relevant ancilliary information, is provided in Table 1. Photometry spanning infrared wavelengths have been assembled from various literature sources including IRAS (Neugebauer et al. 1984), *Akari* (Ishihara et al. 2010), *WISE* (Wright et al. 2010), *Spitzer* (Chen et al. 2006, 2014), and *Herschel* (Riviere-Marichalar et al. 2014). We also determine an upper limit to the millimetre flux of the disc based on a non-detection of the disc (and star) in an archival ALMA Band 6 imaging observation (project 2013.1.01147.S, P.I. S. Perez), using the pipeline reduced imaging data obtained from the Japanese Virtual Observatory.[1]

2.2 HIPPI/-2 aperture polarimetry

We obtained multiwavelength optical and near-infrared aperture polarimetry observations of HD 172555 and a number of interstellar calibration stars using the HIPPI (Bailey et al. 2015) and its successor[2] (HIPPI-2; Bailey et al. 2020a) on the 3.9-m AAT. HIPPI has been successfully used for a range of science programs including surveys of polarization in bright stars (Cotton et al. 2016a), the first detection of polarization due to rapid rotation in hot stars (Cotton et al. 2017a); reflection from the photospheres of binary stars (Bailey et al. 2019) and the most sensitive searches for similar effects from exoplanets (Bott et al. 2016, 2018); and studies of the polarization in active dwarfs (Cotton et al. 2017b, 2019b), debris discs (Cotton et al. 2017b), the interstellar medium (Cotton et al. 2017b, 2019a), and hot dust (Marshall et al. 2016). HIPPI-2 has recently been used in the study of reflected light in binary systems (Bailey et al. 2019; Cotton et al. 2020a), the rapidly rotating system α Oph (Bailey et al. 2020b), the red supergiant Betelgeuse (Cotton et al. 2020b), and the polluted white dwarf G29-38 (Cotton et al. 2020c).

Mounted at the AAT f/8 Cassegrain focus, the HIPPI aperture has a diameter of 6.6 arcsec, such that the disc of HD 172555 lies fully within it (With HIPPI-2 an aperture corresponding to 11.9 arcsec was selected). The observations were taken over four observing runs spanning 2015 May 24–2018 September 1.

HIPPI-class polarimeters achieve very high precision through the use of a ferro-electric liquid crystal (FLC) modulator operating at 500 Hz to beat seeing noise. On the AAT, HIPPI-2 demonstrates a wavelength dependant ultimate precision, ranging from ∼1 part-per-million (ppm) at red wavelengths, ∼ 2 ppm at green wavelengths, and ∼13 ppm for a passband with an effective wavelength of 400 nm, with HIPPI-2 typically achieving a precision 1 ppm better than HIPPI in any given band (Bailey et al. 2020a).

We made observations in six different filter bands: two short-pass filters below 425 (425SP) and 500 nm (500SP) respectively, SDSS g' and r',[3] a Johnson V filter, and a long-pass filter above 650 nm (650LP). These were paired with either blue-sensitive (B) Hamamatsu H10720-210 modules which have ultrabialkali photocathodes or red sensitive (R) Hamamatsu H10720-20 modules with extended red multialkali photocathodes as detectors. The same MS series polarization rotator from boulder non-linear systems was used as a modulator for all of the reported observations with both versions of the instrument. The modulator's performance has drifted over time, from having a wavelength of peak efficiency of 494.8 nm in 2014 to 595.4 nm at the end of the 2018 August run. Our use of the modulator has therefore been broken down into performance eras, the characteristics of which are described in Bailey et al. (2020a) and the supplementary materials of Bailey et al. (2019). The bandpass model uses the characteristics of the optical components, the airmass, and source spectrum, to calculate the band effective wavelength ($\lambda_{\rm eff}$) and modulation efficiency (Eff.) for each observation. A raw observation is multiplied by the inverse of Eff. to give the true polarization.

An observation with HIPPI/-2 consists of four measurements of the target at instrumental position angles of 0°, 45°, 90°, and 135°, with an accompanying sky measurement also made at each position angle. The sky background is first subtracted, and then the measurements combined to eliminate instrumental polarization. The observations are then rotated from the instrumental frame to the sky frame by reference to measurements of high-polarization standard stars. The standards, whose details are given in Bailey et al. (2020a), have uncertainties of about a degree. These high-polarization standard observations are made in either g' or without a filter. However, because of drift in the modulator performance, second-order corrections of 5.°8 and 2.°6 were needed for the 500SP and 425SP filter measurements for the 2018AUG run, based on multiband standard observations. A small wavelength-dependent polarization is imparted by the telescope (TP), which must be determined by the measurement of unpolarized standard stars, and then subtracted. The TP is determined as the mean of all standards observed in a given band, equally weighted. Thence, the error in the TP is incorporated into the errors in the measurements of science targets as the square root of the sum of the errors squared. On occasion, the TP has been stable across consecutive runs, and in such cases observations from both are included in the adopted TPs. A summary of standard observations relevant to the observations made here and some additional details are presented in Appendix A.

[1] Japanese Virtual Observatory

[2] HIPPI-2 has been developed based on experience with HIPPI and Mini-HIPPI (Bailey, Cotton & Kedziora-Chudczer 2017).

[3] Two different versions of the g' and r' filters were used; the Astrodon generation 2 versions were used with HIPPI-2.

Table 1. Stellar parameters.

Parameter	Value	Ref.
Right Ascension (*hms*)	18 45 26.90	1
Declination (*dms*)	−64 52 16.5	1
Proper motions (mas yr^{-1})	32.073, −150.182	1
Distance (pc)	28.34 ± 0.18	1
V (mag)	7.513 ± 0.005	2
$B - V$ (mag)	0.200 ± 0.016	2
Spectral type	A7 V	3
Luminosity ($L_\odot$)	8.093 ± 0.062	1
Radius ($R_\odot$)	$1.55^{+0.17}_{-0.02}$	1
Temperature (K)	7816^{+60}_{-397}	1
Surface gravity, log g	4.18	3
Metallicity [Fe/H]	0.09	3
$v \sin i$ (km s^{-1})	2.0 ± 4.2	3
Age (Myr)	23 ± 2	4

References. (1) Gaia Collaboration et al. (2018); (2) Høg et al. (2000); Gontcharov (2006); (4) Mamajek & Bell (2014).

Observations (Table 2) were made of both HD 172555 and a number of other nearby stars to investigate the properties of the interstellar medium. These interstellar control stars, listed above the line in Table 3,[4] were selected on the basis that they lay within 10° of HD 172555 on the sky, had approximately the same distance ($\delta d \sim 10$ per cent), exhibited no evidence of infrared excess (through cross matching with infrared catalogues), and were of spectral types unlikely to exhibit intrinsic polarization (Cotton et al. 2016a,b, 2017b). Distances were taken from Gaia Collaboration et al. (2018), spectral types from Gray et al. (2006), and V magnitudes from Høg et al. (2000).

The summary of the HIPPI/-2 polarization observations of HD 172555 and the interstellar calibrators given in Table 2 present the data in the form of normalized Stokes parameters $q = Q/I$ and $u = U/I$, along with the internal error of the observations (σ_o). To obtain the true error, σ, the instrumental precision in the corresponding band, σ_i, needs to be added as $\sigma = \sqrt{\sigma_o^2 + \sigma_i^2}$. The polarization, p, can be calculated as $p = \sqrt{q^2 + u^2}$ and the polarization position angle, θ, as $\theta = (1/2)\tan^{-1}(u/q)$. When considering p, since it is positive definite, it is common to debias it according to

$$\hat{p} = \begin{cases} \sqrt{p^2 - \sigma_p^2} & \text{for } p > \sigma_p \\ 0 & \text{for } p < \sigma_p \end{cases}. \quad (1)$$

3 INTERSTELLAR POLARIZATION

3.1 Polarization versus distance

An accurate interstellar subtraction is critical for investigating the polarization properties of a debris disc system. In the case of HD 172555, this task is made easier by the existence of imaging data that can separate the polarization of the disc and the star – allowing the interstellar polarization to be found. The imaging data are monochromatic though, so the wavelength dependence of the interstellar polarization still needs to be determined in order to carry out an interstellar subtraction in other bands.

Fig. 1 shows the polarization in g' of the interstellar controls (and a few intrinsically unpolarized stars from Cotton et al. (2017b)) compared to HD 172555. HD 172555 is more polarized in terms of polarization versus distance (p/d) than any of the nearby stars. The two closest stars (in terms of angular separation, HD 173168 and HD 167425) are more polarized than most of those near the Sun seen in earlier work (Bailey, Lucas & Hough 2010; Cotton et al. 2016a; Marshall et al. 2016; Cotton et al. 2017b), being more than double the p/d predicted by the model in Cotton et al. (2017b) for stars within 25 pc. These two stars, and HD 162521 – which is similarly polarized – have very similar polarization angles to HD 172555. Other nearby stars, in particular HD 177389, are not so polarized showing the ISM in this region is patchy, which prevents firm conclusions being drawn on the interstellar polarization of HD 172555 from this data alone. On balance though, it suggests a large fraction of the polarization is interstellar.

3.2 Wavelength dependence

The wavelength dependence of interstellar (linear) polarization is given by the empirically determined Serkowski law (Serkowski, Mathewson & Ford 1975) as

$$\frac{p(\lambda)}{p_{\max}} = \exp\left[-K \ln^2\left(\frac{\lambda_{\max}}{\lambda}\right)\right], \quad (2)$$

where $p(\lambda)$ is the polarization at wavelength λ, and $p_{\max}$ is the maximum polarization occurring at wavelength $\lambda_{\max}$. The dimensionless constant K describes the inverse width of the polarization curve peaked around $\lambda_{\max}$; Serkowski et al. (1975) gave its value as 1.15. Wilking et al. (1980) later described K in terms of a linear function of $\lambda_{\max}$. Using this form, Whittet et al. (1992) find K to be

$$K = (0.01 \pm 0.05) + (1.66 \pm 0.09)\lambda_{\max} \quad (3)$$

(where $\lambda_{\max}$ is given in μm) – the form of equation (2) that uses this relation is referred to as the Serkowski–Wilking law. There have been only three studies which have determined $\lambda_{\max}$ for stars near to the Sun. In the most recent multiobject study, Cotton et al. (2019a) found 350 ± 50 nm for four stars within the Local Hot Bubble, and 550 ± 20 nm for two stars in its wall. Earlier Marshall et al. (2016) found $\lambda_{\max}$ to be between 35 and 600 nm with a most probable value of 470 nm from two-band observations of a few stars at Southern declinations. Lastly, in investigating the rotational properties of α Oph, Bailey et al. (2020b) found 440 ± 110 nm for that star.

Multiband data were taken for HD 167425 and HD 162521. As stars with similar p/d, θ, d, and small separations from HD 172555, they were chosen as proxies to investigate its interstellar polarization wavelength dependence. The same methods and procedure as followed in Cotton et al. (2019a) were adopted for this purpose. Using a full bandpass model we use PYTHON'S CURVE_FIT program to fit both the Serkowski–Wilking law (K not fit) and the Serkowski law (K fit). The method fits $p_{\max}$ for both control stars, along with $\lambda_{\max}$, and in the latter case K as well. The results are graphed in Fig. 2, and the fit values reported in Table 4.

The Serkowski and Serkwoski–Wilking law fits are similarly good, as judged by the reduced χ^2 statistic, and the values of each fit parameter agree within the stated uncertainties. The values of $p_{\max}$, and hence p/d are higher than was expected for this part of the interstellar medium, and may indicate a transition region between the bulk Local Hot Bubble and its wall (insomuch as these regions are useful as concepts). The Serkowski law gives a redder, more tightly defined $\lambda_{\max}$, but K is not particularly well defined. The past studies of the interstellar medium (Marshall et al. 2016; Cotton et al.

[4]The stars listed below the line are those from the *Interstellar List* in Cotton et al. (2017b) that are within 35° angular separation.

Table 2. HIPPI/-2 polarization measurements of HD 172555 and its interstellar calibrators.

Target	UT	Run	Instr.	Ap. (arcsec)	Mod. era	Fil	PMT	$\lambda_{\rm eff}$ (nm)	Eff.	q (ppm)	u (ppm)
HD 172555	2015-05-25 04:47:17[a]	2015MAY	HIPPI	6.6	E1	425SP	B	400.4	0.569	-17.0 ± 25.6	154.3 ± 26.0
HD 172555	2015-05-25 15:14:49	2015MAY	HIPPI	6.6	E1	425SP	B	400.2	0.568	-68.9 ± 20.0	110.8 ± 19.7
HD 172555	2018-08-27 11:27:42	2018AUG	HIPPI-2	11.9	E6	500SP	B	440.4	0.479	-103.9 ± 7.9	106.2 ± 8.2
HD 172555	2018-08-27 11:59:25	2018AUG	HIPPI-2	11.9	E6	500SP	B	440.4	0.479	-105.5 ± 7.6	112.6 ± 7.9
HD 172555	2018-08-27 12:29:52	2018AUG	HIPPI-2	11.9	E6	g'	B	466.1	0.643	-96.5 ± 6.0	117.6 ± 6.0
HD 172555	2015-05-24 17:53:44	2015MAY	HIPPI	6.6	E1	g'	B	467.2	0.899	-111.5 ± 7.0	110.6 ± 7.1
HD 172555	2018-08-28 14:39:16	2018AUG	HIPPI-2	11.9	E7	V	B	534.3	0.898	-103.8 ± 8.6	91.7 ± 8.1
HD 172555	2018-08-28 15:06:53	2018AUG	HIPPI-2	11.9	E7	V	B	534.4	0.898	-110.5 ± 8.0	94.3 ± 8.3
HD 172555	2015-05-24 18:33:20	2015MAY	HIPPI	6.6	E1	r'	B	599.8	0.833	-125.2 ± 19.2	110.5 ± 18.7
HD 172555	2018-08-26 13:09:54	2018AUG	HIPPI-2	11.9	E6	r'	R	623.2	0.922	-103.7 ± 6.2	86.6 ± 6.3
HD 172555	2018-08-26 13:36:58	2018AUG	HIPPI-2	11.9	E6	r'	R	623.3	0.922	-102.7 ± 6.1	93.0 ± 5.8
HD 172555	2018-08-23 10:37:43	2018AUG	HIPPI-2	11.9	E5	650LP	R	722.3	0.738	-97.6 ± 10.6	91.2 ± 10.5
HD 172555	2018-08-24 11:47:30	2018AUG	HIPPI-2	11.9	E6	650LP	R	722.3	0.775	-87.9 ± 10.2	83.6 ± 10.6
HD 172555	2018-08-26 12:15:13	2018AUG	HIPPI-2	11.9	E6	650LP	R	722.3	0.775	-109.7 ± 10.1	91.5 ± 10.4
HD 172555	2018-08-26 12:42:00	2018AUG	HIPPI-2	11.9	E6	650LP	R	722.3	0.775	-116.4 ± 10.3	67.8 ± 9.5
HD 162521	2018-08-29 10:15:34	2018AUG	HIPPI-2	11.9	E7	500SP	B	443.8	0.457	-93.0 ± 18.2	73.9 ± 18.2
HD 162521	2018-08-29 10:46:09	2018AUG	HIPPI-2	11.9	E7	500SP	B	443.8	0.457	-59.3 ± 17.9	67.8 ± 18.3
HD 162521	2018-08-21 15:22:52	2018AUG	HIPPI-2	11.9	E5	g'	B	470.3	0.737	-106.7 ± 16.7	83.3 ± 15.9
HD 162521	2018-08-29 11:16:41	2018AUG	HIPPI-2	11.9	E7	g'	B	469.0	0.608	-94.5 ± 13.1	48.5 ± 12.6
HD 162521	2018-08-29 11:45:44	2018AUG	HIPPI-2	11.9	E7	V	B	535.7	0.901	-95.5 ± 18.1	73.5 ± 18.2
HD 162521	2018-08-29 12:13:53	2018AUG	HIPPI-2	11.9	E7	V	B	535.7	0.901	-88.5 ± 17.2	62.5 ± 18.3
HD 162521	2018-09-01 14:16:39	2018AUG	HIPPI-2	11.9	E7	650LP	R	724.1	0.860	-91.3 ± 26.2	-2.1 ± 24.0
HD 162521	2018-09-01 14:34:07	2018AUG	HIPPI-2	11.9	E7	650LP	R	724.1	0.861	-25.5 ± 27.5	63.1 ± 25.2
HD 162521	2018-09-01 14:56:18	2018AUG	HIPPI-2	11.9	E7	650LP	R	724.1	0.861	-83.7 ± 18.2	40.7 ± 19.3
HD 165499	2018-08-22 15:53:00	2018AUG	HIPPI-2	11.9	E5	g'	B	472.4	0.748	33.2 ± 11.7	23.6 ± 11.6
HD 167425	2018-08-27 13:52:13	2018AUG	HIPPI-2	11.9	E6	500SP	B	446.4	0.522	-105.9 ± 16.4	72.6 ± 16.4
HD 167425	2018-08-27 14:21:50	2018AUG	HIPPI-2	11.9	E6	500SP	B	446.6	0.523	-85.1 ± 16.2	113.6 ± 16.1
HD 167425	2018-08-22 15:32:12	2018AUG	HIPPI-2	11.9	E5	g'	B	471.7	0.744	-115.0 ± 15.3	80.3 ± 12.7
HD 167425	2018-08-27 14:50:42	2018AUG	HIPPI-2	11.9	E6	g'	B	471.5	0.677	-104.6 ± 13.2	68.0 ± 13.7
HD 167425	2018-08-24 13:42:16	2018AUG	HIPPI-2	11.9	E6	r'	R	625.5	0.920	-90.8 ± 12.6	62.6 ± 12.6
HD 167425	2018-08-26 14:32:21	2018AUG	HIPPI-2	11.9	E6	r'	R	625.6	0.920	-136.9 ± 13.7	82.6 ± 13.1
HD 167425	2018-08-24 13:17:05	2018AUG	HIPPI-2	11.9	E6	650LP	R	725.1	0.766	-102.9 ± 17.5	79.7 ± 16.6
HD 167425	2018-08-26 14:06:48	2018AUG	HIPPI-2	11.9	E6	650LP	R	725.1	0.766	-79.3 ± 18.3	72.6 ± 16.6
HD 173168	2017-06-25 13:25:23	2017JUN	HIPPI	6.6	E2	g'	B	467.5	0.875	-153.1 ± 9.1	159.2 ± 9.0
HD 177389	2018-08-21 15:01:19	2018AUG	HIPPI-2	11.9	E5	g'	B	474.8	0.761	4.9 ± 10.5	-12.9 ± 9.8
HD 186219	2015-10-20 10:37:17	2015OCT	HIPPI	6.6	E1	g'	B	466.6	0.898	78.3 ± 8.3	22.8 ± 8.3

[a]Half of this observation was made on each of two consecutive nights at similar airmass, 2019-05-24 and 2019-05-25.

Table 3. Interstellar calibrators for HD 172555.

Calibrator	V (mag)	Sp. type	d (pc)	Sep (°)
HD 162521	6.36	F5 V	35.52 ± 0.05	5.2
HD 165499	5.47	G0 V	17.75 ± 0.04	4.8
HD 167425	6.17	F9.5 V	23.05 ± 0.21	3.0
HD 173168	5.70	A8 V	65.25 ± 0.31	5.0
HD 177389	5.31	K0 IV	36.98 ± 0.12	4.3
HD 186219	5.39	A4 IV	43.42 ± 0.27	9.5
HD 2151	2.79	G0 V	7.46 ± 0.01	27.0
HD 156384	5.89	K3 V + K5 V	6.84 ± 0.40	32.6
HD 165135	2.99	K0 III	29.70 ± 0.16	35.0
HD 209100	4.69	K5 V	3.64 ± 0.00	24.7

2019a; Bailey et al. 2020b) have found values of $\lambda_{\rm max}$ more closely aligned with the Serkowski–Wilking law fit, and so values of $\lambda_{\rm max}$ equal to 472.6 nm and K equal to 0.79 are adopted.

3.3 Interstellar subtraction

To remove the interstellar polarization, we make the assumptions that the interstellar polarization is described by the Serkowski–Wilking law, has a consistent orientation with wavelength, and that the intrinsic polarization of the star–disc system has a consistent orientation with wavelength too. That is, if the interstellar polarization is removed the remaining polarization can be rotated such that u' is 0 in all bands. We consider the 650LP observations to be equivalent to the SPHERE VBB band observations, given their similar $\lambda_{\rm eff}$, 725 and 735 nm respectively, so in this case, q' should also match the measured integrated disc+star polarization reported by Engler et al. (2018) of 62 ± 8 ppm.

To carry out the subtraction, θ_i, $p_{\rm max}$, and $\theta_\star$ – where the subscripts i and $\star$ represent, respectively, interstellar and intrinsic – need to be determined. This is done using a PYTHON CURVE_FIT-based program that tries to minimize the difference between a set of model values and the data as modified by a function.

Initial values for the program are $p_{\rm max} = 135.4$ ppm and $\theta_i = 59.^\circ5$, chosen based on, respectively, an average of the p/d of HD 161521 and HD 167425 and the interstellar model in Cotton et al. (2017b),

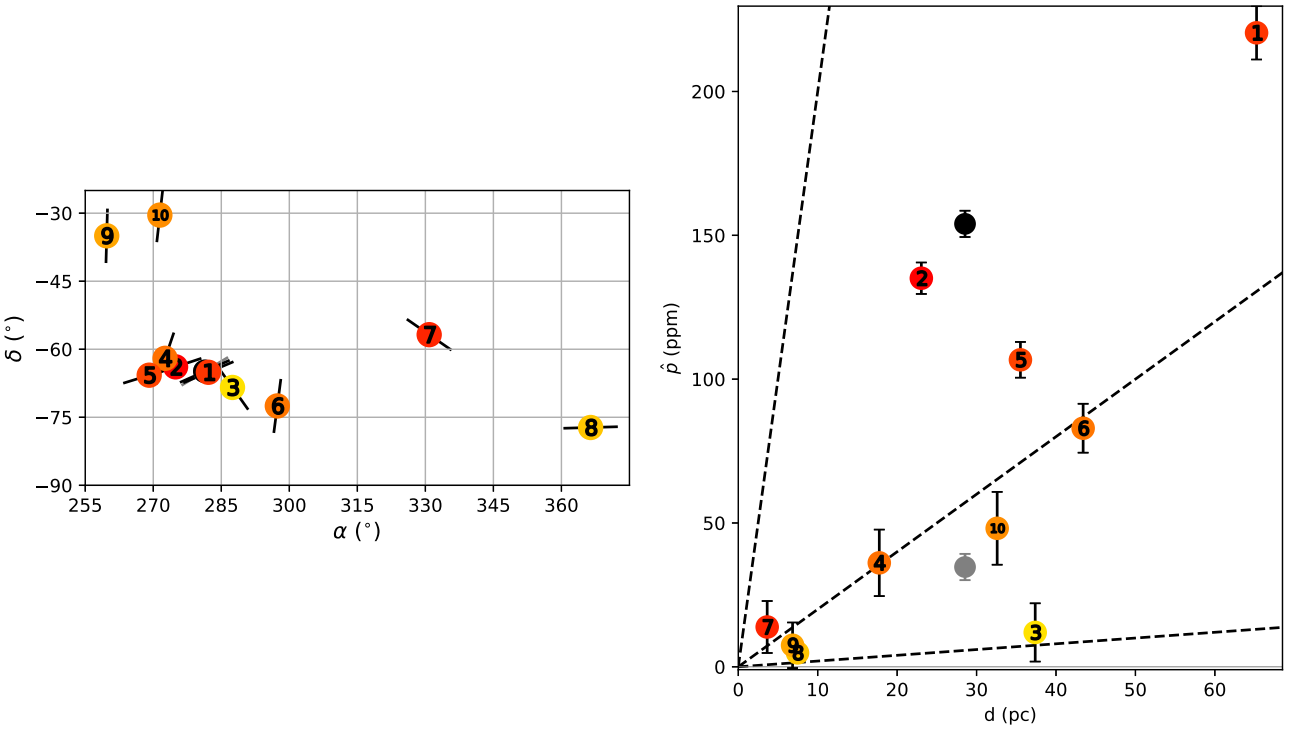

Figure 1. Left-hand panel: polarization as a function of sky position. Unintrinsically polarized stars within 35° of HD 172555 (black) are shown as circles with their position angles (clockwise from north to east) as bars; their colours from red to yellow are encoded based on $\hat{p}/d$, with the numbers indicating their order in terms of separation. The model θ as calculated from Cotton et al. (2017b) for HD 172555 is shown in grey. The stars are (1) HD 173168, (2) HD 167425, (3) HD 177389, (4) HD 165499, (5) HD 162521, (6) HD 186219, (7) HD 209100, (8) HD 2151, (9) HD 156384, and (10) HD 165135. Right-hand panel: (debiased) polarization as a function of distance. The object colours and numbers are as per the left-hand panel, with the grey circle indicating the model interstellar polarization calculated as in Cotton et al. (2017b). The three dashed lines show polarization increasing at 0.2, 2.0, and 20 ppm pc^{-1}.

and $\theta_\star = 22.^\circ3$ based on 90° minus the disc position angle[5] of $112.^\circ3 \pm 1.^\circ5$ found by Engler et al. (2018). The CURVE_FIT program then carries out the following steps with each iteration of fit parameters:

(i) Takes the raw observational data and subtracts q_i and u_i from each band, based on the bandpass calculation of the Serkowski–Wilking law described interstellar polarization with λ_{max} of 472.6 nm, K of 0.79, and p_{max} and θ_i chosen by that CURVE_FIT iteration.

(ii) Rotates the remaining (intrinsic) polarization by $\theta_\star$ into a new frame (q', u').

(iii) Returns u' for each observation, and for the 650LP observations also $62 - q'$, for comparison with model values of 0 [the q' errors are modified to incorporate the uncertainty in the Engler et al. (2018) measurement].

Table 5 summarizes the fit results, whereas Table 6 presents band averaged (error weighted) values for the intrinsic polarization of the system, i.e. that remaining after the interstellar subtraction. The result is a p/d similar to that of HD 167425, a value of $\theta_\star$ consistent with that of Engler et al. (2018), and values of u' consistent with zero to close to 1σ or better in each band, which all give us confidence in the determination.

A fit allowing λ_{max} to be free was also tried, but in that case, the value shifts to ∼400 nm – equivalent to the 425SP λ_{eff} – in order to eliminate the residual in u' in the shortest wavelength band, in so doing the value of p_{max} is pushed up to less realistic levels and $\theta_\star$ is reduced such that it is no longer consistent with the value obtained by Engler et al. (2018). It is prudent not to overemphasize the 425SP band, given that one of the 425SP observations is a composite of two measurements, and the associated error may be underestimated. Consequently, we favour the fit with fixed λ_{max}.

[5]For small grains and a symmetric disc, the polarization is expected to be perpendicular to the major axis.

4 MODELLING

In this section, we attempt to model the ISM-subtracted aperture polarimetry measurements from HIPPI/-2 using the constraint of the observed disc orientation and architecture from the SPHERE measurements. We begin by fitting the dust continuum emission with a debris disc of the dust spatial distribution observed in scattered light (Engler et al. 2018), and inferred grain properties derived from the mid-infrared spectrum (Lisse et al. 2009; Johnson et al. 2012). Following that, we proceed with a simple scattering model of the disc to determine the best-fitting dust grain size for the multiwavelength polarimetric measurements, using the dust optical constants consistent with the composition derived from the spectral energy distribution (SED) fitting to infer the grain size necessary to produce the observed polarization spectrum. Through this two-step approach, we demonstrate that the polarimetric measurements can provide additional, unique information to assist in the interpretation of debris dust.

4.1 Spectral energy distribution

We use the 3D Monte Carlo radiative transfer code HYPERION (Robitaille 2011) to model the dust continuum emission. We again

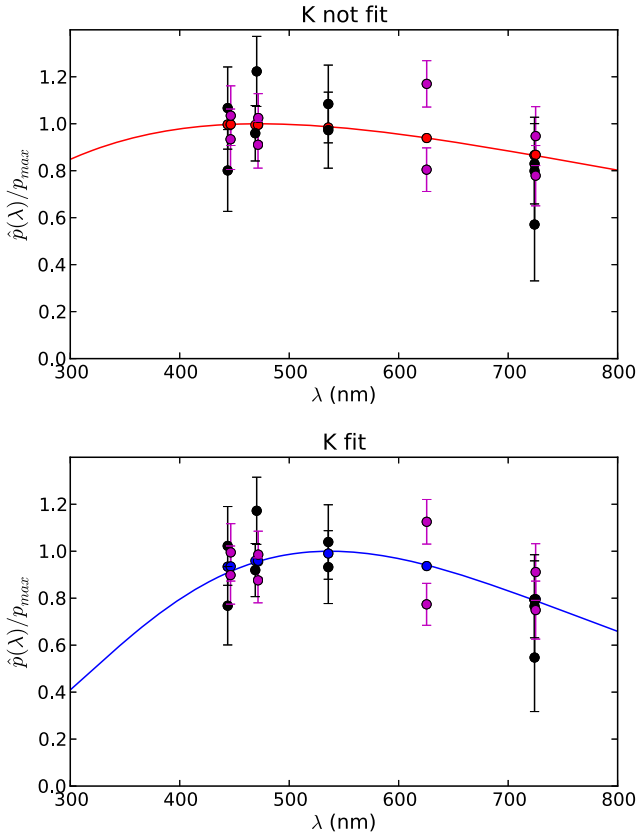

Figure 2. The results of Serkowski fits to two targets – HD 162521 (black) and HD 167425 (magenta). In both panels, $p_{\max}$ is fit for each target, along with $\lambda_{\max}$, in the lower panel K is also fit. The data points in black and magenta are shown as fractional polarization, $\hat{p}/p_{\max}$, for the target, and placed at the effective wavelength $\lambda_{\rm eff}$ for the band. The fit Serkowski curves are shown in red (without K) and blue (with K); the corresponding coloured points correspond to the fits for the bands corresponding to the data points.

Table 4. Serkowski fits to interstellar polarization calibrator stars.

Fit K	$p_{\max}$ (ppm)		$\lambda_{\max}$ (nm)	K	χ^2_r
	HD 162521	HD 167425			
No	109.9 ± 7.1	148.9 ± 7.4	472.6 ± 79.0	0.79[a]	1.10
Yes	114.6 ± 9.8	141.6 ± 10.3	537.2 ± 33.8	2.63 ± 2.12	1.12

[a]Calculated using equation (3).

Table 5. A summary of fit parameters for HD 172555 interstellar subtraction.

$p_{\max}$ (ppm)	$\lambda_{\max}$[a] (nm)	K[a]	θ_i (°)	$\theta_\star$ (°)
176.6 ± 12.1	472.6	0.79	82.5 ± 1.5	$21.5^b \pm 4.5$

[a] Not fit.
[b]This implies a disc position angle of $111.^\circ5 \pm 4.^\circ5$.

adopt the best-fitting parameters for the scattered light disc imaged in Engler et al. (2018) as the parameters for the disc density distribution. We have therefore tacitly assumed that the same dust grains that produce the dust continuum emission are responsible for the scattering and polarization. The objective of this exercise is to demonstrate that the assumed properties of the dust based on spatially unresolved spectroscopic and polarimetric observations provide an adequate fit to the data when combined with the imaged spatial extent of the disc.

Table 6. Band-averaged intrinsic polarization for HD 172555.

Band		n	$\lambda_{\rm eff}$ (nm)	q' (ppm)	u' (ppm)
425SP	B	2	400.3	143.8 ± 18.4	-19.4 ± 18.4
500SP	B	2	440.4	90.6 ± 7.0	2.9 ± 7.2
g'	B	2	466.6	95.4 ± 4.7	5.6 ± 4.8
V	B	2	534.4	76.4 ± 5.9	-5.8 ± 5.8
r'	B	1	599.8	72.6 ± 19.3	23.7 ± 18.8
r'	R	2	623.3	73.2 ± 4.4	-4.0 ± 4.3
650LP	R	4	722.3	$62.4^a \pm 5.2$	1.6 ± 5.1

[a]Fitted to a value of 62 ± 8 ppm based on SPHERE VBB ($\lambda_{\rm eff} = 735$ nm) measurements.

We compare the continuum emission model to a dust SED assembled from available photometric measurements of HD 172555 covering optical to millimetre wavelengths (Høg et al. 2000; Skrutskie et al. 2006; Wright et al. 2010; Ishihara et al. 2010; Chen et al. 2014; Riviere-Marichalar et al. 2014). A summary of the measurements are provided in Table 7. We also extracted photometry from the *Spitzer*/IRS spectrum published in Chen et al. (2006) to constrain the dust composition in the fitting, taking 14 values evenly distributed between 6 and 34 μm.

The stellar photospheric contribution to the total emission was represented by a stellar atmosphere model from the NEXTGEN grid (Allard, Homeier, & Freytag 2012) taken from the Spanish Virtual Observatory (Rodrigo, Solano, & Bayo Arán 2017) with an effective temperature of 7800 K, surface gravity $\log(g)$ of 4.2 (interpolated from $\log(g)$ 4.0 and 4.5), and Solar metallicity, which are appropriate values for HD 172555 (see Table 1). The photosphere model was scaled to provide a total luminosity of 8.093 $L_\odot$.

The SED fitting process was carried out in the following manner; given that the disc spatial extent and dust size distribution are fixed, the only constraint left is to determine the dust composition that best replicates the SED. The radial dust density distribution is given by a functional form

$$\rho = \rho_0 \times ((R/R_0)^{-2\alpha_{\rm in}} + (R/R_0)^{-2\alpha_{\rm out}})^{-0.5} \times (1 + (z/(z_0(R/R_0)^\beta))^2)^{-1}, \quad (4)$$

where ρ is the dust density at a given position around the star, ρ_0 is a density scaling factor, R is the radial distance from the star, R_0 is the radial distance of the peak in disc emission from the star, $\alpha_{\rm in}$ and $\alpha_{\rm out}$ are the exponents for the slope of the disc interior and exterior to the peak position, z is the vertical distance from the disc mid-plane, z_0 is the value of z at R_0, and β is the flaring index of the disc. Following Engler et al. (2018), the parameters for the disc density distribution in the model are $R_0 = 11.3$ AU, $\alpha_{\rm in} = -3.5$, $\alpha_{\rm out} = 6.8$, $z_0 = 0.6$ AU, and $\beta = 0.40$.

For the dust physical properties, we assume a power-law size distribution of grains between $a_{\rm min}$ and $a_{\rm max}$ (i.e. $dn \propto a^{-q}da$). We fix the minimum and maximum grain sizes for the dust as $a_{\rm min} = 0.01$ μm and $a_{\rm max} = 1$ mm. The exponent of the size distribution q was also fixed to be 3.95. Although a more physically motivated size distribution would omit grains in the range $0.1 < a < 1.0$ μm from the radiative transfer modelling, due to their rapid removal by radiation pressure, we adopt a single power-law size distribution as this is still consistent with the observations as presented in Johnson et al. (2012) and simplifies the modelling process.

Table 7. Photometric measurements of HD 172555 used in the SED fitting.

Wavelength (μm)	Flux density (mJy)	Telescope/ instrument	Reference
0.44	43 915 ± 615	Johnson *B*	Høg et al. (2000)
0.55	45 112 ± 406	Johnson *V*	Høg et al. (2000)
1.20	28 270 ± 7350	2MASS *J*	Skrutskie et al. (2006)
1.64	21 530 ± 4564	2MASS *H*	Skrutskie et al. (2006)
2.16	12 727 ± 394	2MASS K_S	Skrutskie et al. (2006)
3.4	5658 ± 1398	*WISE* W1	Wright et al. (2010)
4.6	4038 ± 670	*WISE* W2	Wright et al. (2010)
9	1229 ± 75	*Akari*/IRC9	Ishihara et al. (2010)
12	1032 ± 62	*WISE* W3	Wright et al. (2010)
18	947 ± 52	*Akari*/IRC18	Ishihara et al. (2010)
22	1520 ± 525	*WISE* W4	Wright et al. (2010)
24	947 ± 83	*Spitzer*/MIPS24	Chen et al. (2014)
70	226 ± 16	*Spitzer*/MIPS70	Johnson et al. (2012)
70	191 ± 13	*Herschel*/PACS70	Riviere-Marichalar et al. (2014)
100	79 ± 6	*Herschel*/PACS100	Riviere-Marichalar et al. (2014)
160	32 ± 2	*Herschel*/PACS160	Riviere-Marichalar et al. (2014)
1300	<0.240	ALMA Band 6	This work

For the dust optical properties, we assemble optical constants (*n*, *k*) from the Jena database of optical constants for cosmic dust (Jäger et al. 2003) for the materials used in Lisse et al. (2009) to match the mid-infrared spectrum of HD 172555. Not all the materials utilized in the spectrum fitting presented in Table 2 of Lisse et al. (2009) had (*n*, *k*) values available through accessible online data bases, but we obtained values for the following species: Al_2O_3 (Zeidler et al. 2001), $MgSiO_3$ and Mg_2SiO_4 (Jäger et al. 2003), $MgFeSiO_4$ (Jäger et al. 1994, Dorschner et al. 1995), Fe_2SiO_4 (Fabian et al. 2001), FeO and MgO (Henning et al. 1995), MgFeS (Begemann et al. 1994), SiO and SiO_2 (Henning & Mutschke 1997), and C (Jäger et al. 1998). The dust composition fit undertaken here should not therefore be directly compared to that work for consistency. Having obtained (*n*, *k*) values for a range of materials, we then extrapolate the optical constants beyond the available wavelength ranges by extrapolation down to 0.1 μm and up to 2 mm, using the linear slope of the first (or last) two data points for the measured optical constants to extend the range. Using these extrapolated optical constants we run individual disc models through HYPERION, assuming the previously determined disc spatial extent and dust size distribution for all materials, an appropriate material density assuming the grains are hard compact spheres, and a scaling density ρ_0 of $\approx 10^{-19}$ g cm^{-3} for the individual material SED models, which was adjusted so that each individual SED represented emission from the same mass of dust, in this case 3.45×10^{23} g.

To reproduce the observed SED we use the affine-invariate Markov chain Monte Carlo code EMCEE (Foreman-Mackey et al. 2013) to determine the appropriate mixture of the components by assigning the SED of each individual mineral species a weighting factor between 10^{-3} and 10^{3} (i.e. between −3 and 3 in log space) and then calculating the least-squares fit of the weighted combination of individual species' SEDs to the observations. The weighting factors for each species were initialized at 1 (0 in log space), with the individual walkers given a small scatter of 0.05 about this value. We used 200 walkers and 1000 steps (200 000 realizations) to deduce the maximum probability weightings for the materials, discarding the first 400 steps of each chain before calculating the probability distribution to extract the 16th, 50th, and 84th percentile values. The results of the fitting process are presented in Figure 3, with a summary of the weighting factors given in Table 8. It should be noted that these weightings are relative to the reference SED of each component, and are therefore not expected to add up to unity. In Appendix B, we provide SEDs of the individual materials, and a plot of the relative contribution of these components to the total model.

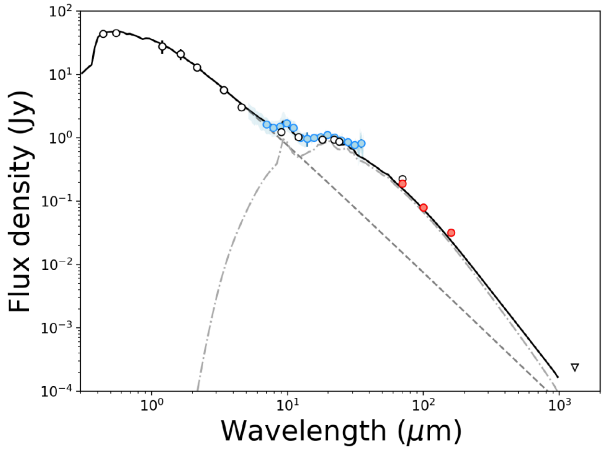

Figure 4. Plot of flux density versus wavelength for HD 172555. The disc model was calculated based on the disc architecture from the SPHERE images (Engler et al. 2018), and the grain size distribution inferred from fitting the mid-infrared spectrum (Johnson et al. 2012). The stellar photosphere model is represented by the grey dashed line, the total disc contribution (all 11 components) by the grey dot–dashed line, and the total emission (star + disc) as the solid black line. The blue line represents the *Spitzer*/IRS spectrum (Chen et al. 2006), and photometry extracted from the mid-infrared spectrum are represented as blue circular data points. Red circular data points denote *Herschel*/PACS photometry (Riviere-Marichalar et al. 2014). An upper limit from ALMA Band 6 is denoted by an inverted triangle.

From the dust composition fitting, we can infer the appropriate optical constants to use in the polarization spectrum modelling for consistency between all elements of this analysis. The composition analysis is somewhat degenerate, and the relative weightings of different species tied to the sampling of different regions of the mid-infrared spectrum (e.g. denser sampling across the 10- or 20-μm

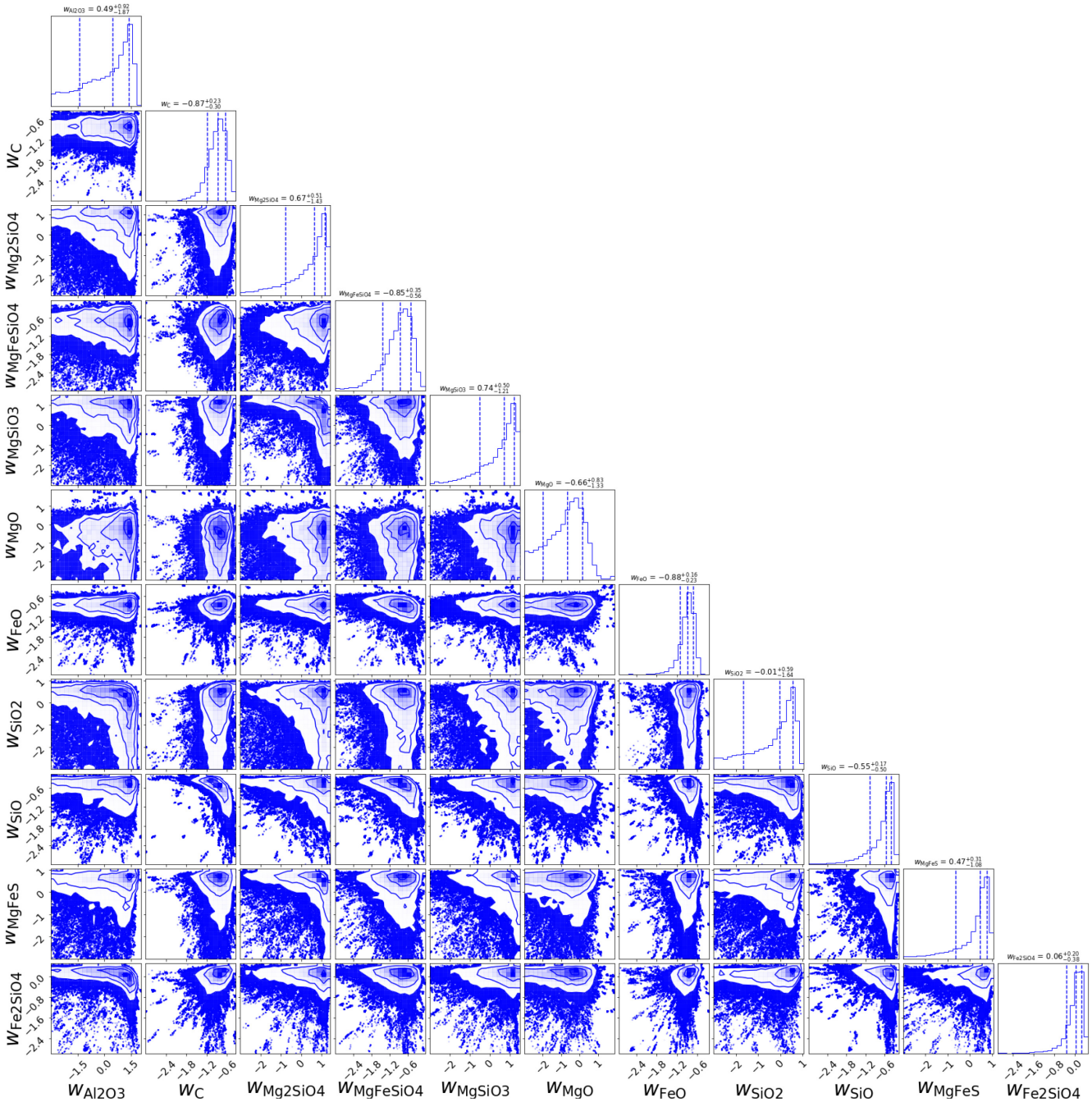

Figure 3. Corner plot showing the probability distributions of the weights of 11 mineral species to HD 172555's SED; see the text for details. The species fitted were (shown from the left- to right-hand side): Al_2O_3, C, Mg_2SiO_4, $MgFeSiO_4$, $MgSiO_3$, MgO, FeO, SiO_2, SiO, MgFeS, and Fe_2SiO_4. The values for the weightings are given in Table 8.

feature gives different maximum probabilities for the various components). Our fitting results place strong constraints on the weighting on four of the species examined here, namely C, $MgFeSiO_4$, SiO, and MgFeS. There are weaker constraints on the weightings for the remaining seven species, several of which have long tails, or broad peaks, to their posterior probability distributions highlighting the degeneracy in the spectral fitting presented here.

A comparison of the model SED with observations of HD 172555 is presented in Figure 4. The model is consistent, within uncertainties, with the mid-infrared spectrum across its full extent, reproduces the far-infrared photometry, and falls below the millimetre-wavelength upper limit. We have therefore obtained general good agreement between model emission calculated using the weighted sums of the individual dust models and the observations. We have used a single dust grain size distribution with a power-law exponent of 3.95 as has been previously found to reproduce the SED for HD 172555's disc (e.g. Chen et al. 2006; Lisse et al. 2009; Johnson et al. 2012). We find this adequately represents the data in combination with the additional spatial constraint of Engler et al. (2018).

Table 8. Summary of the material weights determined by fitting of a composite SED of 11 materials to the SED and mid-infrared spectrum.

Species	log (Wgt)	Mass (10^{-5} $M_\oplus$)
Aluminium oxide, Al_2O_3	$0.49^{+0.93}_{-1.90}$	$17.83^{+133.15}_{-17.61}$
Carbon, C	$-0.88^{+0.24}_{-0.31}$	$0.77^{+0.55}_{-0.39}$
Forsterite, Mg_2SiO_4	$0.66^{+0.51}_{-1.46}$	$26.70^{+60.60}_{-25.77}$
Olivine, $MgFeSiO_4$	$-0.85^{+0.36}_{-0.57}$	$0.81^{+1.04}_{-0.59}$
Fayalite, Fe_2SiO_4	$0.05^{+0.20}_{-0.38}$	$6.51^{+3.82}_{-3.80}$
Ortho-enstatite, $MgSiO_3$	$0.73^{+0.51}_{-1.22}$	$31.04^{+69.25}_{-29.19}$
Magnesium oxide, MgO	$-0.68^{+0.87}_{-1.34}$	$1.19^{+7.09}_{-1.13}$
Iron oxide, FeO	$-0.89^{+0.16}_{-0.23}$	$0.75^{+0.34}_{-0.31}$
Silicon dioxide, SiO_2	$-0.02^{+0.59}_{-1.66}$	$5.54^{+16.04}_{-5.24}$
Silicon oxide, SiO	$-0.55^{+0.17}_{-0.50}$	$1.63^{+0.78}_{-1.12}$
Magnesium iron sulphide, MgFeS	$0.47^{+0.30}_{-1.10}$	$16.98^{+17.24}_{-15.62}$

Note. Total dust mass of the disc (in grains up to 1 mm) is inferred to be 1.10×10^{-3} $M_\oplus$, or 7.19×10^{21} kg.

4.2 Polarimetry

We model the HIPPI/-2 aperture polarization measurements using the disc architecture and orientation of the scattered light disc imaged in Engler et al. (2018). The albedo and scattering Müller matrix for each composition was calculated using a parallelized FORTRAN95 implementation of BHMie.[6] We calculate the disc polarization using a 3D model of the disc density distribution combined with the dust optical constants, following the model presented in Scicluna et al. (2015). We assume the measured polarization is produced in single scattering events for dust grains in the optically thin disc redirecting unpolarized starlight toward the observer. The scattering angles for a 3D volume containing the disc (centred on the star) are calculated to generate linear fractional polarization (q and u) values at 200 wavelengths between 0.3 and 0.9 μm. Polarization measurements of the disc (as projected on to the plane of the sky) were determined using the ratio of Müller matrix elements S_{11} and S_{12}, the dust albedo, and the stellar flux. The orientation of the disc in the model is chosen such that the degree of polarization in the U vector is zero by default.

We proceed by generating model polarization spectra for each dust composition spanning 0.3–0.9 μm, sampling 200 wavelengths within this range, for minimum dust grains sizes between 0.01 and 6.5 μm. We fixed the maximum grain size as 1 mm, with a power-law size distribution exponent of −3.95, as per the radiative transfer modelling. We did not omit grains with sizes 0.1–1.0 μm from the scattering polarization calculation despite these grains being swiftly removed by radiation forces. If such grains were shown to be capable of reproducing the observed polarization, it would be an intriguing result given that they would be expected to be transitory in the disc around HD 172555.

Whilst the radiative transfer modelling used grains smaller than 0.3 μm to generate the dust emission, such grains are weakly polarizing (Marshall et al. 2016; Kirchschlager et al. 2017), and would not be expected to produce an adequate fit to the polarimetry, so we curtail the parameter space of our search accordingly. Similarly, dust grains larger than 5 μm would not be expected to produce strongly polarized light at shorter wavelengths setting the upper boundary to the range of grain sizes considered here. We also calculate polarization spectra for astronomical silicate dust grains (Draine 2003) as a point of comparison to the dust composition determined from this work.

[6]https://github.com/pscicluna/bhmie

We calculate a single model polarization spectrum for each grain size using the weightings calculated in the dust grain radiative transfer modelling. The best-fitting grain size was then determined using a least-squares fit of the model polarization spectrum for each grain size to the multiwavelength polarimetry. A bandpass model was used to calculate synthetic HIPPI/-2 polarimetric measurements across the model spectra at the relevant wavelengths for the fitting process.

We found a satisfactory fit to the polarization using dust grains with n, k values calculated from a dust composition determined from the relative weights of the 11 components used in the SED fitting. The best-fitting polarization model using this dust composition has a minimum grain size $a_{\rm min} = 3.89$ μm and is an adequate match to the observations, as shown in Figure 5. The model polarization spectra do not replicate the steep rise in polarimetric signal toward shorter wavelengths, but are consistent within the substantial uncertainties attached to the magnitude and shape of the model polarization spectra at those shortest wavelengths.

With the astronomical silicate models, we find a best-fitting minimum grain size $a_{\rm min} = 1.25$ μm from a least-squares fit between the grain size dependent polarization spectra and the observations. The dust grain size we infer from this simple model is comparable to the radiation blow-out grain size for HD 172555 ($a_{\rm blow} \approx 1.5$ μm) and consistent with the best-fitting grain size derived from the radiative transfer models. From this result, combined with that of the mixed composition, we infer that the dust grains responsible for the polarization are not the very smallest grains that dominate the overall disc surface area and from which the mid-infrared spectral features originate.

5 DISCUSSION

5.1 Technique

Previously published aperture polarization measurements at the 10^{-5}–10^{-4} rms polarization level have not convincingly detected signatures of dust polarization from debris disc host stars (García & Gómez 2015; Vandeportal et al. 2019). The fundamental difficulty in applying the technique to debris discs is separating the interstellar polarization from that due to the debris disc. Ordinarily, the fractional polarization from a debris disc system will not exceed half of the associated continuum flux excess. A dust fractional excess ($L_{\rm dust}/L_\star$) of 10^{-4} would only be expected to yield a polarimetric signal of a

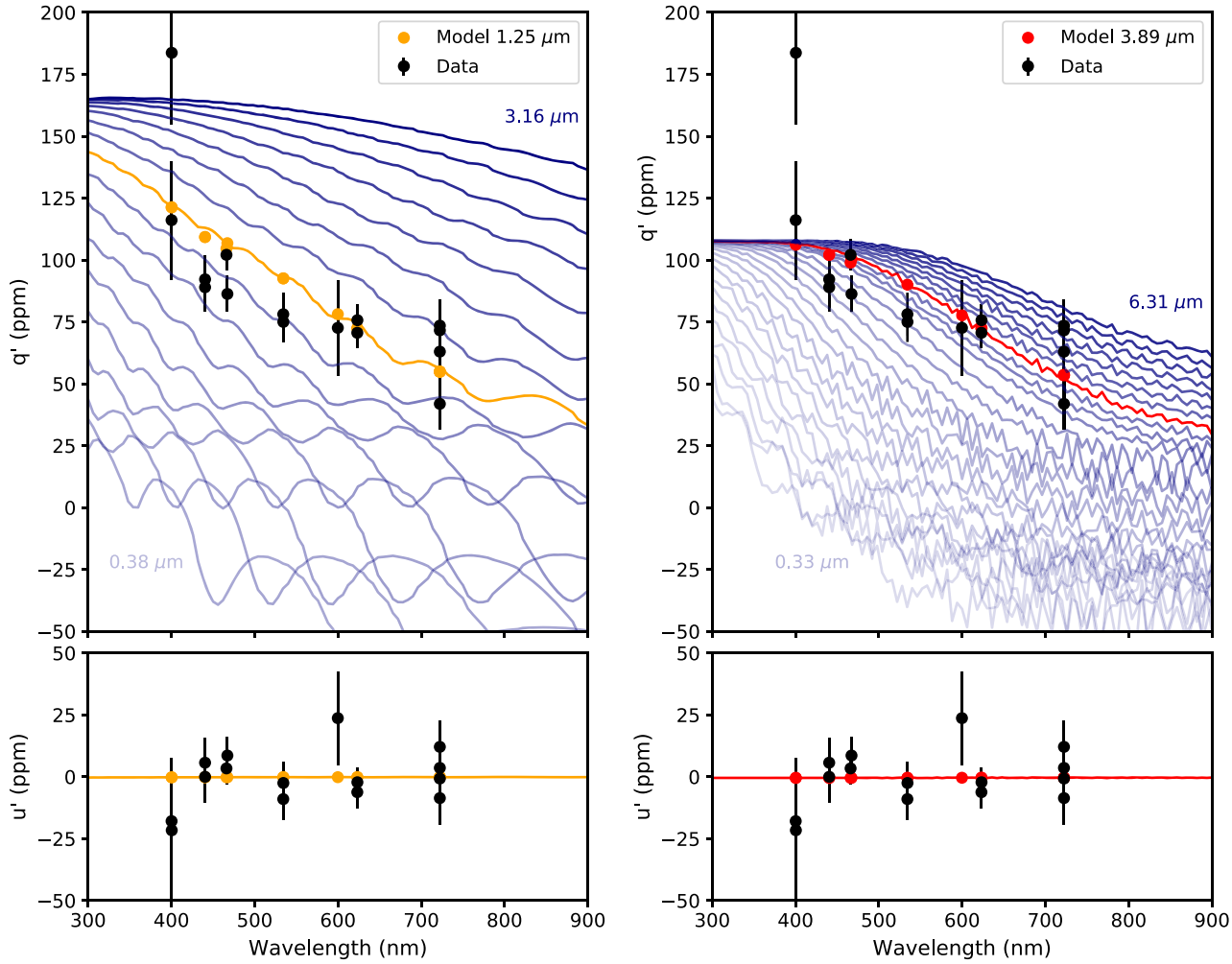

Figure 5. Plots of wavelength versus linear polarization vectors $q^{'}$ (top panels) and $u^{'}$ (bottom panels) for the best-fitting models of astronomical silicate (left-hand panels) and radiative transfer derived dust composition (right-hand panels) following the assumed disc architecture and dust grain properties (see the text for details). The polarization spectra for the best-fitting dust grain size for astronomical silicate (mixed composition) are denoted by the yellow (red) line, with the waveband derived polarimetric measurements denoted by coloured dots. Polarization spectra for adjacent dust grain sizes are given as shaded blue lines ([0.33,] 0.38, 0.43, 0.49, 0.56, 0.64, 0.73, 0.84, 0.96, 1.09, 1.25, 1.43, 1.63, 1.86, 2.12, 2.42, 2.77, 3.16, [3.39, 3.63, 3.89, 4.17, 4.47, 4.79, 5.13, 5.50, 5.89, 6.31] μm), and the observations are shown as black dots.

few $\times$ 10^{-5} (depending on the assumed grain shape and porosity). This means that only the brightest discs have been detectable up until now. Scattered light detections of debris discs have established that the continuum emission and scattered light from a given disc do not always correlate (e.g. Schneider et al. 2014), and debris dust grains generally have low albedoes (<0.1) comparable to that of bodies in the Edgeworth–Kuiper belt (Choquet et al. 2018; Marshall et al. 2018). These factors reduce the expected scattered light brightness of debris dust, further reducing their overall detectability in polarization.

The development of parts-per-million (10^{-6}) polarimeters has helped with this (Bailey et al. 2010; Wiktorowicz et al. 2010a,b; Cotton et al. 2016a, 2017b, 2020c), but interstellar polarization contributions are typically tens of ppm within the Local Hot Bubble (within 75–150 pc, Bailey et al. 2010; Cotton et al. 2016a, 2017b; Piirola et al. 2020), and hundreds of ppm just beyond it (Cotton et al. 2019b; Gontcharov & Mosenkov 2019). Consequently, to characterize the disc polarization, the interstellar polarization must be removed. The task is made more difficult since the wavelength dependence of interstellar polarization within the Local Hot Bubble is not yet well defined (Marshall et al. 2016; Cotton et al. 2019b). Our results with regard to the interstellar medium here, where we obtain $\lambda_{max} = 472.6 \pm 79.0$ nm for HD 162521 and HD 167425 combined, serve to improve this situation.

A similar problem exists in aperture polarimetry of other non-variable phenomena, for instance, in determining the inclination and rotation rate of rapidly rotating stars (Cotton et al. 2017a; Bailey et al. 2020b). That case is more easily dealt with, however, since the wavelength dependence of polarization intrinsic to the system is well defined (Bailey et al. 2020b). Whereas in debris disc systems we do not yet understand their architectures or compositions well enough to so easily constrain the parameters; consequently, observations of the target system alone are not sufficient.

Imaging polarimetry of discs has been possible for the brightest discs with favourable (generally edge-on) orientations to the line of sight for some time, e.g. β Pic (Gledhill, Scarrott & Wolstencroft 1991; Krivova, Krivov & Mann 2000; Tamura et al. 2006) and

AU Mic (Graham, Kalas & Matthews 2007). New instruments such as the Gemini Planet Imager (e.g. Esposito et al. 2020) and SPHERE-ZIMPOL (e.g. HR 4796A; Milli et al. 2019) have increased the number of such systems investigated. As related here for HD 172555, these allow the removal of the interstellar component. Furthermore, by occluding the largely unpolarized central star they reduce its fractional contribution to insignificance. Of course being able to map polarization through the disc has its own advantages. However, there are also disadvantages; imaging is easier at red and infrared wavelengths where adaptive optics can be effective, and the occulting disc will obscure the dust nearest the star along with it. Multiband measurements at optical wavelengths are particularly important for elucidating the nature of the dust in disc systems.

5.2 Dust properties

We have attempted to match the multiwavelength aperture polarimetry measurements reported here using a simple polarization model with dust grain scattering properties based on the size distribution and optical properties determined by Mie theory based on both the composition inferred from the radiative transfer modelling and astronomical silicate.

Our model manages to replicate the overall wavelength dependence of the observed polarization properties of the disc except for the shortest wavelengths. We have thus been able to find a single comprehensive solution for the dust continuum emission and polarization observations for HD 172555. This is perhaps surprising, given the number of simplifying assumptions, including the adoption of Mie theory to calculate the dust grain optical properties, which is well known to poorly replicate polarimetric dust signatures. The best-fitting minimum grain size with a dust composition based on the radiative transfer modelling was $a_{\rm min} = 3.89$ μm. Using the astronomical silicate composition, we obtain a best-fitting minimum grain size of 1.25 μm. Our analysis is strongly suggestive that $\sim$ micron-sized grains, larger than the radiation blow-out size, are responsible for the observed polarization. This rules out small, submicron grains that are responsible for the mid-infrared spectral features as the origin of the polarization. This is consistent with the generally seen result in SED modelling that the minimum grain size around later type stars is a few times the blow out limit from radiation pressure.

However, the assumptions inherent in this work used to calculate the optical constants from the composition model and regarding the dust grain shape prevent us placing a tight constraint on the exact size of dust grains responsible for the polarimetric signal. In particular, n, k measurements for dust species spanning the full range of wavelengths present in the observations were not always available. This required extrapolation to fill in the blanks, in some cases across important regions for interpreting scattered light and polarization. Comprehensive, broad wavelength (0.1 μm–1 mm) coverage of dust optical constants for astronomically interesting species would be an invaluable resource, particularly across a range of temperatures relevant for circumstellar disc studies (tens to hundreds K).

6 CONCLUSIONS

We have undertaken a multiwavelength study of the dust continuum emission and optical polarimetric properties of the HD 172555 debris disc system. We determine that the previously posited dust composition and grain size distribution (Chen et al. 2006; Lisse et al. 2009; Johnson et al. 2012) are consistent with the new spatial constraint imposed by scattered light imaging (Engler et al. 2018).

We have convincingly detected polarization from a debris disc using aperture polarimetry for the first time, demonstrating the consistency of our measurements with those of imaging polarization at comparable wavelengths. The measurements presented here illustrate the need for parts-per-million sensitivity to undertake such an analysis.

We constrain the dust grain size responsible for the observed polarization (under the assumption of Mie theory and astronomical silicate composition) to be around 1.25 μm, and 3.89 μm for grains with optical constants derived from the dust composition used to fit the SED. The smallest grains in the disc, i.e. those responsible for the mid-infrared spectral features and which dominate the disc surface area, are not the ones responsible for the observed polarization from the disc. We are able to replicate the polarimetric observations of HD 172555 with our model using a single dust composition and grain size with a composition derived from the radiative transfer modelling. However, this result requires more rigorous testing with scattering from non-spherical dust grains and a more realistic grain size distribution including the effects of radiation pressure, for example. Here we have demonstrated a unique methodology that uses the complimentary nature of imaging and aperture techniques to refine our understanding of the debris dust in this system. As such, this is a showcase of the synergy of imaging and aperture polarimetric techniques.

ACKNOWLEDGEMENTS

The authors thank the anonymous referee for their insightful and detailed comments which helped improved the article.

This research has made use of the SIMBAD data base, operated at CDS, Strasbourg, France.

This research has made use of NASA's Astrophysics Data System.

This research has made use of the Spanish Virtual Observatory (http://svo.cab.inta-csic.es) supported from the Spanish MICINN/FEDER through grant AyA2017-84089, namely the Spectral Stellar Libraries services developed by the Spanish Virtual Observatory in the framework of the IAU Comission G5 Working Group : Spectral Stellar Libraries.

This paper has made use of the PYTHON packages ASTROPY (Astropy Collaboration et al. 2013, 2018), SCIPY (Jones et al. 2001), MATPLOTLIB (Hunter 2007), EMCEE (Foreman-Mackey et al. 2013), CORNER (Foreman-Mackey 2016), and HYPERION (Robitaille 2011).

We thank Dag Evensberget for assisting with observations in 2018 August.

The development of HIPPI was funded by the Australian Research Council through Discovery Projects grant DP140100121 and by the UNSW Faculty of Science through its Faculty Research Grants program. Funding for the construction of HIPPI-2 was provided by UNSW through the Science Faculty Research Grants Program. We thank the staff of the AAT for their support for our observing programme.

JPM acknowledges research support by the Ministry of Science and Technology of Taiwan under grants MOST104-2628-M-001-004-MY3, MOST107-2119-M-001-031-MY3, and MOST109-2112-M-001-036-MY3, and Academia Sinica under grant AS-IA-106-M03.

This paper makes use of the following ALMA data: ADS/JAO.ALMA#2013.1.01147.S. ALMA is a partnership of ESO (representing its member states), NSF (USA), and NINS (Japan), together with NRC (Canada), MOST and ASIAA (Taiwan), and KASI (Republic of Korea), in cooperation with the Republic of Chile. The Joint ALMA Observatory is operated by ESO, AUI/NRAO, and NAOJ. The ALMA data used in this work were retrieved from the JVO portal (http://jvo.nao.ac.jp/portal/) operated by ADC/NAOJ.

DATA AVAILABILITY

The data underlying this study are available in this paper and in its online supplementary material.

REFERENCES

Allard F., Homeier D., Freytag B., 2012, Philosophical Transactions of the Royal Society A: Mathematical, Physical and Engineering Sciences, 370, 2765
Astropy Collaboration et al., 2013, A&A, 558, A33
Astropy Collaboration et al., 2018, AJ, 156, 123
Bailey J., Cotton D. V., Howarth I. D., Lewis F., Kedziora-Chudczer L., 2020b, MNRAS, 494, 2254
Bailey J., Cotton D. V., Kedziora-Chudczer L., 2017, MNRAS, 465, 1601
Bailey J., Cotton D. V., Kedziora-Chudczer L., De Horta A., Maybour D., 2019, Nat. Astron., 3, 636
Bailey J., Cotton D. V., Kedziora-Chudczer L., De Horta A., Maybour D., 2020a, Publ. Astron. Soc. Aust., 37, e004
Bailey J., Kedziora-Chudczer L., Cotton D. V., Bott K., Hough J. H., Lucas P. W., 2015, MNRAS, 449, 3064
Bailey J., Lucas P. W., Hough J. H., 2010, MNRAS, 405, 2570
Begemann B., Dorschner J., Henning Th., Mutschke H., Thamm E., 1994, ApJ, 423, 71
Bott K., Bailey J., Cotton D. V., Kedziora-Chudczer L., Marshall J. P., Meadows V. S., 2018, AJ, 156, 293
Bott K., Bailey J., Kedziora-Chudczer L., Cotton D. V., Lucas P. W., Marshall J. P., Hough J. H., 2016, MNRAS, 459, L109
Chen C. H., Mittal T., Kuchner M., Forrest W. J., Lisse C. M., Manoj P., Sargent B. A., Watson D. M., 2014, ApJS, 211, 25
Chen C. H. et al., 2006, ApJS, 166, 351
Choquet É. et al., 2018, ApJ, 854, 53
Cotten T. H., Song I., 2016, ApJS, 225, 15
Cotton D. V., Bailey J., Horta A. D., Norris B. R. M., Lomax J. R., 2020b, Res. Notes AAS, 4, 39
Cotton D. V., Bailey J., Howarth I. D., Bott K., Kedziora-Chudczer L., Lucas P. W., Hough J. H., 2017a, Nat. Astron., 1, 690
Cotton D. V., Bailey J., Kedziora-Chudczer L., Bott K., Lucas P. W., Hough J. H., Marshall J. P., 2016a, MNRAS, 455, 1607
Cotton D. V., Bailey J., Kedziora-Chudczer L., Bott K., Lucas P. W., Hough J. H., Marshall J. P., 2016b, MNRAS, 460, 18
Cotton D. V., Bailey J., Kedziora-Chudczer L., De Horta A., 2020a, MNRAS, 497, 2175
Cotton D. V., Bailey J., Pringle J. E., Sparks W. B., von Hippel T., Marshall J. P., 2020c, MNRAS, 494, 4591
Cotton D. V., Marshall J. P., Bailey J., Kedziora-Chudczer L., Bott K., Marsden S. C., Carter B. D., 2017b, MNRAS, 467, 873
Cotton D. V. et al., 2019a, MNRAS, 483, 1574
Cotton D. V. et al., 2019b, MNRAS, 483, 3636
Dorschner J., Begemann B., Henning Th., Jäger C., Mutschke H., 1995, A&A, 300, 503
Draine B. T., 2003, ApJ, 598, 1017
Engler N., Schmid H. M., Quanz S. P., Avenhaus H., Bazzon A., 2018, A&A, 618, A151
Esposito T. M. et al., 2020, AJ, 160, 24
Fabian D., Henning Th., Jäger C., Mutschke H., Dorschner J., Wehran O., 2001, A&A, 378, 228
Foreman-Mackey D., 2016, J. Open Source Softw., 1, 24
Foreman-Mackey D., Hogg D. W., Lang D., Goodman J., 2013, PASP, 125, 306
Gaia Collaboration et al., 2018, A&A, 616, A1
García L., Gómez M., 2015, Rev. Mex. Astron. Astrofis., 51, 3
Gledhill T. M., Scarrott S. M., Wolstencroft R. D., 1991, MNRAS, 252, 50P
Gontcharov G. A., 2006, Astron. Lett., 32, 759
Gontcharov G. A., Mosenkov A. V., 2019, MNRAS, 483, 299
Grady C. A., Brown A., Welsh B., Roberge A., Kamp I., Rivière Marichalar P., 2018, AJ, 155, 242
Graham J. R., Kalas P. G., Matthews B. C., 2007, ApJ, 654, 595
Gray R. O., Corbally C. J., Garrison R. F., McFadden M. T., Bubar E. J., McGahee C. E., O'Donoghue A. A., Knox E. R., 2006, AJ, 132, 161
Henning Th., Begemann B., Mutschke H., Dorschner J., 1995, Astronomy and Astrophysics Supplement, 112, 143
Henning Th., Mutschke H., 1997, A&A, 327, 743
Hunter J. D., 2007, Comput. Sci. Eng., 9, 90
Høg E. et al., 2000, A&A, 355, L27
Ishihara D. et al., 2010, A&A, 514, A1
Johnson B. C. et al., 2012, ApJ, 761, 45
Jäger C., Il'in V.B., Henning Th., Mutschke H., Fabian D., Semenov D., Voshchinnikov N., 2003, Journal of Quantitative Spectroscopy & Radiative Transfer, 79-80, 765
Jäger C., Mutschke H., Begemann B., Dorschner J., Henning Th., 1994, A&A, 292, 641
Jäger C., Mutschke H., Henning Th., 1998, A&A, 332, 291
Kiefer F., Lecavelier des Etangs A., Augereau J. C., Vidal-Madjar A., Lagrange A. M., Beust H., 2014, A&A, 561, L10
Kirchschlager F., Wolf S., Krivov A. e. V., Mutschke H., Brunngräber R., 2017, MNRAS, 467, 1614
Krivova N. A., Krivov A. V., Mann I., 2000, ApJ, 539, 424
Lisse C. M., Chen C. H., Wyatt M. C., Morlok A., Song I., Bryden G., Sheehan P., 2009, ApJ, 701, 2019
Mamajek E. E., Bell C. P. M., 2014, MNRAS, 445, 2169
Marshall J. P. et al., 2016, ApJ, 825, 124
Marshall J. P. et al., 2018, ApJ, 869, 10
Milli J. et al., 2019, A&A, 626, A54
Moerchen M. M., Telesco C. M., Packham C., 2010, AJ, 723, 1418
Morlok A., Koike C., Tomeoka K., Mason A., Lisse C., Anand M., Grady M., 2012, Icarus, 219, 48
Neugebauer G. et al., 1984, ApJ, 278, L1
Piirola V. et al., 2020, A&A, 635, A46
Riviere-Marichalar P. et al., 2012, A&A, 546, L8
Riviere-Marichalar P. et al., 2014, A&A, 565, A68
Robitaille T. P., 2011, A&A, 536, A79
Rodrigo C., Solano E., Bayo Arán A., 2017, ASI Conference Series, edited by P. Coelho, L. Martins & E. Griffin, 14, 63
Schneider G. et al., 2014, AJ, 148, 59
Scicluna P., Siebenmorgen R., Wesson R., Blommaert J. A. D. L., Kasper M., Voshchinnikov N. V., Wolf S., 2015, A&A, 584, L10
Serkowski K., Mathewson D. S., Ford V. L., 1975, ApJ, 196, 261
Skrutskie M. F. et al., 2006, AJ, 131, 1163
Smith R., Wyatt M. C., Haniff C. A., 2012, MNRAS, 422, 2560
Su K. Y. L., Rieke G. H., Melis C., Jackson A. P., Smith P. S., Meng H. Y. A., Gáspár A., 2020, ApJ, 898, 21
Tamura M., Fukagawa M., Kimura H., Yamamoto T., Suto H., Abe L., 2006, ApJ, 641, 1172
Vandeportal J., Bastien P., Simon A., Augereau J.-C., Storer É., 2019, MNRAS, 483, 3510
Virtanen P. et al., 2020, Nature Methods, 17, 261
Whittet D. C. B., Martin P. G., Hough J. H., Rouse M. F., Bailey J. A., Axon D. J., 1992, ApJ, 386, 562
Wiktorowicz S. J., , Duchene G., Graham J. R., Kalas P., 2010a, In the Spirit of Lyot 2010, University of Paris Diderot, Paris, France
Wiktorowicz S., Graham J. R., Duchene G., Kalas P., 2010b, AAS , 215, 374
Wilking B. A., Lebofsky M. J., Martin P. G., Rieke G. H., Kemp J. C., 1980, ApJ, 235, 905
Wright E. L. et al., 2010, AJ, 140, 1868
Wyatt M. C., Smith R., Su K. Y. L., Rieke G. H., Greaves J. S., Beichman C. A., Bryden G., 2007, ApJ, 663, 365
Zeidler S., Posch Th., Mutschke H., 2013, A&A, 553, A81

APPENDIX A: STANDARD OBSERVATIONS

The instrumental PA is calibrated with reference to high-polarization standard stars observed in g' or without a filter. Table A1 lists the standards observed for each run. The errors associated with the

Table A1. Precision in PA by observing run.

Run	PA standard observations					SD
	HD 23512	147084	154445	160529	187929	(°)
2015MAY	0	4	1	0	0	0.17
2015OCT	1	0	*2*	0	*2*	0.24
2017JUN	0	2	1	1	0	1.11
2018AUG	0	3	0	3	*5*	0.86

Note. All standards were observed in g' except where the number is italicized, in which case one instance was observed without a filter.

Table A2. Multiband PA correction for 2018AUG run.

Band		$\lambda_{\rm eff}$ (nm)	PA standard observations HD: 147084	160529	187929	ΔPA (°)	SD (°)
425SP	B	403.5	1	2	3	2.60	1.08
500SP	B	441.3	1	2	2	5.80	1.27
g'	B	466.9	2	2	3	−0.09	0.87
g'	R	485.7	1	1	1	−0.03	1.21
V	B	537.6	0	2	2	−0.06	0.84
r'	B	603.7	1	2	2	0.64	0.69
r'	R	611.2	1	1	1	0.10	0.85
650LP	R	722.4	1	1	1	0.30	0.70

Note. The observations cover a number of different modulator performance eras.

literature values are around a degree. The column labelled 'SD' gives the standard deviation of $\Delta PA = PA_{\rm obs} - PA_{\rm lit}$, where $PA_{\rm obs}$ is the θ for the observation after calibration, and $PA_{\rm lit}$ the literature value as given in Bailey et al. (2020a). Table A2 shows that for the 2018AUG run 425SP and 500SP observations, after calibration based on g'/Clear, are significantly rotated. A second-order correction was therefore applied.

Tables A3 and A4 list all observations used to calibrate the TP for each run in each band. The polarization of each of these stars is assumed to be zero.

Table A3. HIPPI low polarization standard observations.

Standard	UT	Run	Instr.	Ap. (arcsec)	Mod. era	Fil	PMT	$\lambda_{\rm eff}$ (nm)	Eff (ppm)	q (ppm)	u
HD 48915	2015-05-24 09:09:47	2015MAY	HIPPI	6.6	E1	425SP	B	400.6	0.570	− 67.9 ± 4.1	3.9 ± 3.9
HD 140573	2015-05-23 13:16:51	2015MAY	HIPPI	6.6	E1	425SP	B	407.8	0.602	− 52.0 ± 17.7	− 1.1 ± 17.4
HD 140573	2015-05-25 13:43:21	2015MAY	HIPPI	6.6	E1	425SP	B	407.8	0.602	− 28.7 ± 17.8	18.5 ± 17.4
HD 140573	2015-05-26 13:07:50	2015MAY	HIPPI	6.6	E1	425SP	B	407.8	0.602	− 45.2 ± 14.7	10.2 ± 14.9
HD 140573	2015-06-26 11:43:37	2015JUN	HIPPI	6.6	E1	425SP	B	407.8	0.602	− 24.4 ± 15.7	13.7 ± 15.9
HD 140573	2015-06-27 13:09:02	2015JUN	HIPPI	6.6	E1	425SP	B	408.1	0.603	− 38.8 ± 14.8	66.1 ± 14.9
Adopted TP								406.6		− 42.8 ± 6.1	18.5 ± 6.0
HD 48915	2015-05-23 07:58:16	2015MAY	HIPPI	6.6	E1	g'	B	465.6	0.895	− 38.7 ± 1.3	− 2.1 ± 1.3
HD 48915	2015-05-24 07:58:30	2015MAY	HIPPI	6.6	E1	g'	B	465.8	0.896	− 39.8 ± 0.7	− 0.1 ± 0.7
HD 102647	2015-06-27 08:28:37	2015JUN	HIPPI	6.6	E1	g'	B	466.5	0.897	− 44.0 ± 2.3	1.0 ± 2.3
HD 140573	2015-05-22 11:55:52	2015MAY	HIPPI	6.6	E1	g'	B	476.3	0.918	− 23.8 ± 4.9	18.9 ± 5.1
HD 140573	2015-05-26 12:30:43	2015MAY	HIPPI	6.6	E1	g'	B	475.9	0.917	− 36.0 ± 3.9	6.9 ± 3.9
HD 140573	2015-06-26 12:11:26	2015JUN	HIPPI	6.6	E1	g'	B	475.9	0.917	− 41.7 ± 4.2	− 9.1 ± 4.4
HD 140573	2015-06-27 12:45:15	2015JUN	HIPPI	6.6	E1	g'	B	475.9	0.917	− 27.2 ± 3.8	18.7 ± 3.8
Adopted TP								471.7		− 35.9 ± 1.3	4.9 ± 1.3
HD 48915	2015-05-24 08:14:17	2015MAY	HIPPI	6.6	E1	r'	B	598.9	0.835	− 25.0 ± 1.6	2.5 ± 1.7
HD 140573	2015-05-23 13:42:01	2015MAY	HIPPI	6.6	E1	r'	B	603.7	0.826	− 31.1 ± 7.7	− 5.0 ± 8.0
HD 140573	2015-05-25 13:20:36	2015MAY	HIPPI	6.6	E1	r'	B	603.7	0.826	− 34.0 ± 6.7	0.2 ± 6.7
Adopted TP								602.1		− 30.0 ± 3.4	− 0.7 ± 3.5
HD 2151	2015-10-14 09:42:14	2015OCT	HIPPI	6.6	E1	g'	B	472.5	0.910	− 56.0 ± 3.8	− 2.2 ± 3.8
HD 2151	2015-10-19 13:07:41	2015OCT	HIPPI	6.6	E1	g'	B	472.0	0.909	− 49.8 ± 3.7	− 3.9 ± 3.7
HD 2151	2015-10-29 09:36:13	2015NOV	HIPPI	6.6	E1	g'	B	472.3	0.909	− 54.2 ± 3.8	1.9 ± 3.8
HD 48915	2015-10-16 18:27:29	2015OCT	HIPPI	6.6	E1	g'	B	464.7	0.893	− 51.6 ± 0.7	1.9 ± 0.7
HD 48915	2015-10-19 17:16:09	2015OCT	HIPPI	6.6	E1	g'	B	464.9	0.894	− 48.9 ± 1.0	− 2.9 ± 1.5
HD 48915	2015-11-02 18:08:07	2015NOV	HIPPI	6.6	E1	g'	B	464.7	0.893	− 42.0 ± 0.9	4.4 ± 0.9
Adopted TP								468.5		− 50.4 ± 1.1	− 0.1 ± 1.1
HD 2151	2017-06-25 19:36:07	2017JUN	HIPPI	6.6	E2	g'	B	472.0	0.888	− 21.3 ± 4.2	6.8 ± 4.1
HD 2151	2017-08-10 19:05:57	2017AUG	HIPPI	6.6	E2	g'	B	472.3	0.888	− 16.9 ± 4.2	4.4 ± 4.6
HD 48915	2017-08-11 19:40:30	2017AUG	HIPPI	6.6	E2	g'	B	466.2	0.872	− 21.4 ± 4.8	− 10.3 ± 5.0
HD 48915	2017-08-19 19:00:40	2017AUG	HIPPI	6.6	E2	g'	B	466.2	0.872	2.6 ± 2.7	− 5.7 ± 2.6
HD 102647	2017-06-22 09:03:49	2017JUN	HIPPI	6.6	E2	g'	B	466.5	0.873	− 3.1 ± 2.4	0.7 ± 2.6
HD 102647	2017-06-30 08:26:33	2017JUN	HIPPI	6.6	E2	g'	B	466.5	0.873	− 4.7 ± 2.5	**− 19.9 ± 2.5**
HD 102870	2017-06-23 08:58:12	2017JUN	HIPPI	6.6	E2	g'	B	471.5	0.886	− 10.9 ± 5.2	15.5 ± 4.9
HD 102870	2017-06-25 08:22:44	2017JUN	HIPPI	6.6	E2	g'	B	471.3	0.886	− 3.1 ± 5.9	− 10.5 ± 5.4
Adopted TP								469.1		− 9.9 ± 1.5	− 2.4 ± 1.5

Table A4. HIPPI-2 low polarization standard observations.

Standard	UT	Run	Instr.	Ap.	Mod.	Fil	PMT	$\lambda_{\rm eff}$	Eff	q	u
				(arcsec)	era			(nm)	(ppm)	(ppm)	
HD 2151	2018-07-11 19:00:22	2018JUL	HIPPI-2	11.9	E4	500SP	B	446.4	0.717	−7.7 ± 3.8	32.8 ± 4.2
HD 2151	2018-09-02 16:38:53	2018AUG	HIPPI-2	11.9	E7	500SP	B	446.4	0.474	35.7 ± 6.9	19.0 ± 7.0
HD 10700	2018-07-10 18:51:19	2018JUL	HIPPI-2	11.9	E4	500SP	B	448.2	0.735	−9.5 ± 5.4	7.1 ± 5.1
HD 10700	2018-08-28 16:09:19	2018AUG	HIPPI-2	11.9	E7	500SP	B	448.2	0.490	34.7 ± 7.5	36.3 ± 8.1
HD 48915	2018-08-19 19:33:02	2018AUG	HIPPI-2	11.9	E5	500SP	B	438.6	0.547	7.7 ± 2.6	32.8 ± 2.7
HD 48915	2018-08-27 18:57:03	2018AUG	HIPPI-2	11.9	E6	500SP	B	438.6	0.467	10.2 ± 1.5	0.0 ± 1.6
HD 102647	2018-07-11 09:14:15	2018JUL	HIPPI-2	11.9	E4	500SP	B	440.7	0.682	1.6 ± 2.6	26.1 ± 2.6
HD 102647	2018-07-16 08:57:38	2018JUL	HIPPI-2	11.9	E4	500SP	B	440.7	0.682	−11.4 ± 2.6	10.7 ± 2.7
HD 102870	2018-07-12 08:56:01	2018JUL	HIPPI-2	11.9	E4	500SP	B	446.1	0.716	−18.1 ± 5.6	15.1 ± 5.4
HD 140573	2018-07-17 12:39:21	2018JUL	HIPPI-2	11.9	E4	500SP	B	450.5	0.753	−9.9 ± 4.3	18.4 ± 4.3
HD 140573	2018-08-17 09:41:43	2018AUG	HIPPI-2	11.9	E5	500SP	B	450.1	0.636	−6.3 ± 4.6	4.7 ± 5.4
Adopted TP								445.0		2.5 ± 1.4	18.4 ± 1.5
HD 2151	2018-07-12 18:14:27	2018JUL	HIPPI-2	11.9	E4	g'	B	471.0	0.829	−23.3 ± 2.9	8.5 ± 3.1
HD 2151	2018-09-02 10:19:09	2018AUG	HIPPI-2	11.9	E7	g'	B	472.1	0.627	0.5 ± 4.6	−35.3 ± 4.9
HD 2151	2018-09-02 16:21:37	2018AUG	HIPPI-2	11.9	E7	g'	B	471.0	0.620	−0.1 ± 5.2	17.9 ± 4.7
HD 10700	2018-07-15 19:19:11	2018JUL	HIPPI-2	11.9	E4	g'	B	473.2	0.838	−11.6 ± 4.3	4.7 ± 4.2
HD 10700	2018-08-28 15:35:45	2018AUG	HIPPI-2	11.9	E7	g'	B	473.2	0.633	−14.9 ± 6.0	5.6 ± 5.2
HD 10700	2018-09-02 17:44:04	2018AUG	HIPPI-2	11.9	E7	g'	B	473.2	0.633	−13.7 ± 5.8	10.3 ± 5.9
HD 48915	2018-08-17 19:40:14	2018AUG	HIPPI-2	11.9	E5	g'	B	464.4	0.704	−6.1 ± 1.5	−2.0 ± 1.4
HD 48915	2018-08-20 19:36:03	2018AUG	HIPPI-2	11.9	E5	g'	B	464.4	0.704	−5.7 ± 1.4	−2.5 ± 1.4
HD 102647	2018-07-10 09:16:20	2018JUL	HIPPI-2	11.9	E4	g'	B	466.0	0.809	−21.6 ± 2.1	16.5 ± 1.9
HD 102647	2018-07-11 08:36:01	2018JUL	HIPPI-2	11.9	E4	g'	B	465.5	0.807	−14.1 ± 1.9	10.5 ± 2.0
HD 102870	2018-07-12 08:18:28	2018JUL	HIPPI-2	11.9	E4	g'	B	470.4	0.827	−21.0 ± 4.2	6.2 ± 4.1
HD 140573	2018-07-18 11:26:49	2018JUL	HIPPI-2	11.9	E4	g'	B	475.3	0.847	−19.8 ± 3.1	10.2 ± 3.1
HD 140573	2018-08-16 09:50:15	2018AUG	HIPPI-2	11.9	E5	g'	B	475.3	0.764	−17.1 ± 3.7	4.5 ± 3.6
Adopted TP								470.4		−13.0 ± 1.1	4.2 ± 1.0
HD 2151	2018-07-12 18:34:42	2018JUL	HIPPI-2	11.9	E4	V	B	536.7	0.951	−29.3 ± 4.9	8.1 ± 4.9
HD 10700	2018-07-15 18:59:46	2018JUL	HIPPI-2	11.9	E4	V	B	539.5	0.949	−29.9 ± 6.4	−3.3 ± 6.4
HD 48915	2018-08-16 19:42:31	2018AUG	HIPPI-2	11.9	E5	V	B	533.1	0.952	−5.8 ± 1.7	5.0 ± 1.5
HD 48915	2018-08-27 19:08:28	2018AUG	HIPPI-2	11.9	E6	V	B	533.1	0.934	−17.1 ± 1.3	2.9 ± 1.5
HD 102870	2018-07-17 08:42:01	2018JUL	HIPPI-2	11.9	E4	V	B	536.6	0.951	−32.2 ± 3.6	−4.2 ± 3.4
HD 140573	2018-07-18 12:03:46	2018JUL	HIPPI-2	11.9	E4	V	B	541.3	0.948	−21.2 ± 4.9	13.0 ± 4.6
HD 140573	2018-07-22 13:07:49	2018JUL	HIPPI-2	11.9	E4	V	B	541.6	0.948	−9.9 ± 4.9	−6.6 ± 4.4
HD 140573	2018-08-17 09:59:15	2018AUG	HIPPI-2	11.9	E5	V	B	541.2	0.954	−19.6 ± 4.9	2.4 ± 4.6
Adopted TP								537.9		−20.6 ± 1.6	2.2 ± 1.5
HD 2151	2018-07-23 17:54:47	2018JUL	HIPPI-2	11.9	E4	r'	R	625.6	0.823	−14.3 ± 3.0	4.0 ± 2.9
HD 2151	2018-08-23 16:11:43	2018AUG	HIPPI-2	11.9	E5	r'	R	625.6	0.894	−14.8 ± 3.5	−6.9 ± 3.7
HD 2151	2018-08-24 16:37:59	2018AUG	HIPPI-2	11.9	E6	r'	R	625.6	0.920	−12.8 ± 3.8	−4.5 ± 3.5
HD 2151	2018-08-26 16:44:18	2018AUG	HIPPI-2	11.9	E6	r'	R	625.6	0.920	−16.8 ± 3.1	−6.0 ± 3.4
HD 10700	2018-08-23 16:47:46	2018AUG	HIPPI-2	11.9	E5	r'	R	626.9	0.892	−14.9 ± 4.3	1.5 ± 4.3
HD 10700	2018-08-24 17:24:12	2018AUG	HIPPI-2	11.9	E6	r'	R	626.9	0.918	−3.7 ± 4.2	−0.4 ± 4.3
HD 102647	2018-07-23 08:50:14	2018JUL	HIPPI-2	11.9	E4	r'	R	622.9	0.828	−10.8 ± 3.1	4.9 ± 3.3
HD 102647	2018-07-24 08:39:56	2018JUL	HIPPI-2	11.9	E4	r'	R	622.9	0.828	−1.6 ± 3.2	4.5 ± 3.1
HD 102870	2018-07-23 09:10:07	2018JUL	HIPPI-2	11.9	E4	r'	R	625.7	0.823	−17.3 ± 5.3	13.4 ± 5.3
HD 102870	2018-07-24 09:18:08	2018JUL	HIPPI-2	11.9	E4	r'	R	625.7	0.823	−13.7 ± 5.6	0.6 ± 5.5
HD 140573	2018-08-28 09:48:59	2018AUG	HIPPI-2	11.9	E7	r'	R	627.8	0.956	−16.8 ± 2.8	−4.2 ± 2.6
Adopted TP								625.6		−12.5 ± 1.2	0.6 ± 1.2
HD 2151	2018-08-23 16:28:43	2018AUG	HIPPI-2	11.9	E5	650LP	R	725.2	0.729	−12.5 ± 6.4	−3.7 ± 6.3
HD 2151	2018-08-24 16:57:40	2018AUG	HIPPI-2	11.9	E6	650LP	R	725.2	0.766	−9.5 ± 4.5	2.5 ± 4.4
HD 2151	2018-08-26 17:04:47	2018AUG	HIPPI-2	11.9	E6	650LP	R	725.2	0.766	−16.9 ± 4.3	−4.3 ± 4.3
HD 10700	2018-08-23 17:08:19	2018AUG	HIPPI-2	11.9	E5	650LP	R	728.6	0.724	−11.5 ± 5.5	−8.9 ± 5.8
HD 10700	2018-08-24 17:45:22	2018AUG	HIPPI-2	11.9	E6	650LP	R	728.6	0.761	−3.1 ± 5.5	4.2 ± 6.0
HD 102647	2018-07-23 08:32:24	2018JUL	HIPPI-2	11.9	E4	650LP	R	721.4	0.647	−3.3 ± 5.7	−1.9 ± 5.4
HD 102647	2018-07-24 08:22:46	2018JUL	HIPPI-2	11.9	E4	650LP	R	721.4	0.647	−14.9 ± 5.7	−1.3 ± 5.7
HD 102870	2018-07-23 09:30:33	2018JUL	HIPPI-2	11.9	E4	650LP	R	725.0	0.637	8.3 ± 9.1	12.3 ± 9.1
HD 102870	2018-07-24 08:59:24	2018JUL	HIPPI-2	11.9	E4	650LP	R	725.0	0.637	11.9 ± 8.7	37.4 ± 8.7
HD 140573	2018-08-28 09:28:41	2018AUG	HIPPI-2	11.9	E7	650LP	R	731.5	0.851	−19.5 ± 3.1	2.0 ± 2.9
Adopted TP								725.7		−7.1 ± 1.9	3.8 ± 1.9

APPENDIX B: DUST COMPOSITION MODELS

We take optical constants (n, k) for representative materials from the Jena Database of Optical Constants. These optical constants are extrapolated to cover the wavelength range appropriate for this work. An SED showing the weighted contributions in comparison with each other is presented in Fig. B6, whilst the individual reference SEDs used to calculate weightings for each component's contribution to the observed SED are presented in Fig. B7.

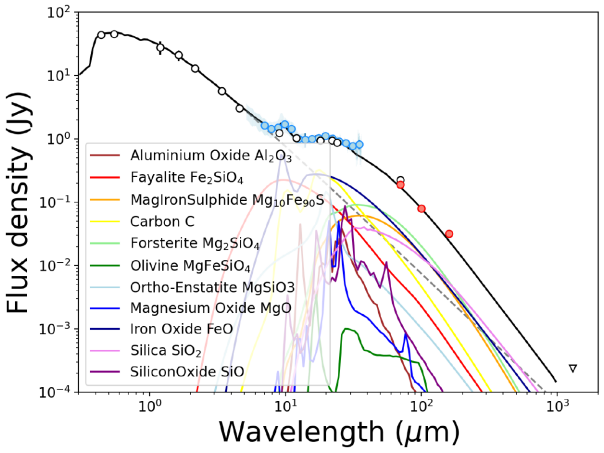

Figure B6. Plot of flux density versus wavelength for HD 172555. The stellar photosphere model (dashed black line), total model (solid black line), and observations (white, blue and red dots, with 1σ uncertainties) are presented alongside the weighted spectra for all 11 dust components fitted to the mid-infrared spectrum and far-infrared photometry. Brown: Al_2O_3, red: C, orange: Mg_2SiO_4, yellow: $MgFeSiO_4$, light green: $MgSiO_3$, green: MgO, light blue: FeO, blue: SiO_2, dark blue: SiO, violet: MgFeS, and purple: Fe_2SiO_4.

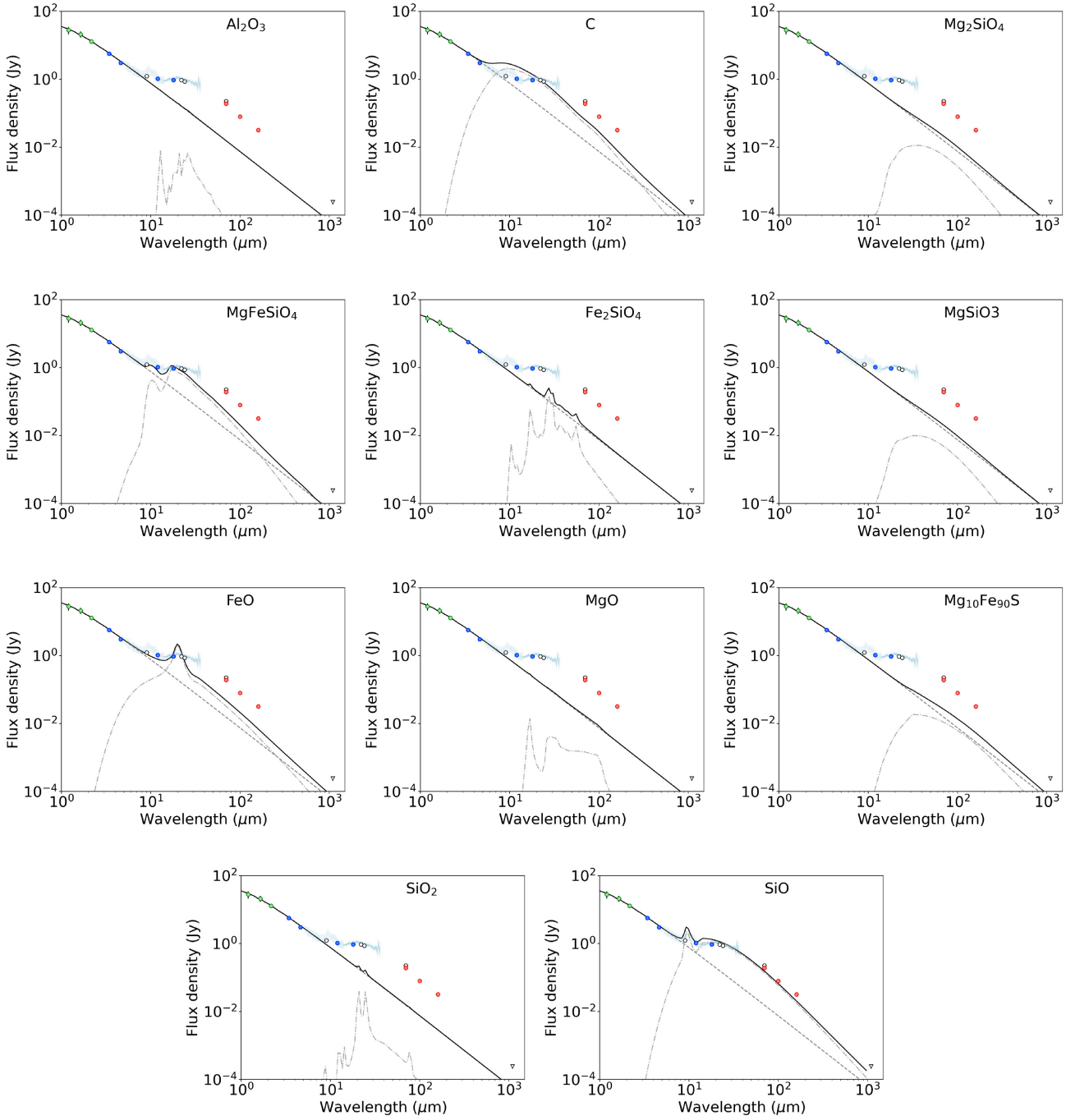

Figure B7. SEDs for the eleven individual mineral species used to model HD 172555's infrared excess. From the top left- to bottom right-hand side, the species are: aluminium oxide, carbon, forsterite, olivine, fayalite, ortho-enstatite, iron oxide, magnesium oxide, magnesium iron sulphide, silicon oxide, and silicon dioxide. The grain size for each species spanned 0.01–1000 μm, with a power-law size distribution exponent of -3.95; the spatial distribution was matched to the scattered light image of Engler et al. (2018). Each SED is scaled to the same dust mass of 3.45×10^{20} kg, or 5.78×10^{-5} $M_{\odot}$. The choice of mass for the SED scaling was arbitrary. Observations are shown by circular data points (upper limit an inverted triangle), as per the main text. The grey dashed line show the stellar photosphere, grey dot–dashed line shows the dust contribution, and the black solid line is the sum of these components.

This paper has been typeset from a TEX/LATEX file prepared by the author.